IEEE Transactions on Robotics (T-RO) paper, presented at ICRA 2026, Vienna, Austria. Cite as T-RO paper.

Augmented Tank-Based Control Guarantees Passive Individual Interaction Environment for Multiuser Haptic-Enabled Robotic Systems

Cui Wang, Yudong Liu, Chenyang Sun, *Member, IEEE*, Ping Li, *Member, IEEE*, Yi-Feng Chen, *Member, IEEE*, Mingjie Dong, *Senior Member, IEEE*, Zhenhong Li, *Senior Member, IEEE*, Lu Liu, *Senior Member, IEEE*, and Mingming Zhang, *Senior Member, IEEE*

***Abstract*—Despite extensive investigations into the multiuser haptic-enabled robotic system (M-Hers), achieving scalable control design in the presence of nonpassive human operators remains a key challenge. This is primarily due to the increasing complexity of stability conditions and interaction coupling as the number of operators grows. In this study, we address this challenge in two steps. First, we introduce the individual interaction environment (IIE) to isolate the passivity violations, which facilitates the independent control design for each human–robot subsystem, thereby enhancing the scalability with respect to the number of subsystems. Second, within the IIE framework, we identify passivity-violating components caused by partners' active behaviors and propose a novel augmented tank-based controller (ATBC) to guarantee passive IIE while maintaining high rendering accuracy. Specifically, the ATBC employs an energy-related power regulation strategy to enhance interaction safety and a time-varying control gain to mitigate the negative effects of power regulation on rendering fidelity. We validated the proposed method through collaborative haptic tasks on a customized M-Hers composed of three robots in four different scenarios. Comparative studies demonstrate that our approach effectively ensures IIE passivity in the presence of active human behaviors, while ensuring high reproducibility and achieving a favorable balance between passivity and rendering accuracy.**

***Index Terms*—Augmented tank-based control, collaborative tasks, energy-related power regulation (EPR), multiuser haptic-enabled robotic system (M-Hers), nonpassive individual interaction environment (IIE).**

I. Introduction

THE multiuser haptic-enabled robotic system (M-Hers) facilitates collaborative tasks by providing real-time kinesthetic feedback across multiple human–robot interaction subsystems. This system has demonstrated a promising potential in applications, including surgical training, telerobotic rehabilitation, and multiplayer gaming. A key feature of these applications is bidirectional energy transfer, where operators simultaneously exert and receive physical energy. For instance, in a virtual surgical environment, each operator exerts control over the task and receives feedback in the form of environment forces, facilitating a realistic training experience [1]. Similarly, in rehabilitation, haptic-enabled robots allow each patient kinesthetically feel the movements generated by other participants, enabling joint participation in the training task. Despite facilitating dynamic interactions, recent studies reveal that human operators often exhibit nonpassive dynamics during voluntary actions, such as intentional force intervention [2] and assistive force generation [3]. These nonpassive behaviors can inject energy into the system beyond its passive constraints, which may make the whole system unstable.

In the context of multiuser haptic interaction, passivity is a powerful tool for analyzing system stability and guiding the design of controllers to ensure stable and safe interaction among users. Methods including wave-variable-based control, immittance matrix-based control, and the time-domain passivity approach (TDPA), rely on the principle that a system composed of passive subsystems interconnected in parallel or feedback structures remains passive [4] and, thus, stable. These methods typically assume that both the environment and human operators exhibit passive behaviors [5], [6]. Based on this assumption, these methods follow a control paradigm in which overall system stability can be guaranteed as long as the interaction network

Received 18 August 2025; revised 13 November 2025; accepted 9 December 2025. Date of publication 12 January 2026; date of current version 23 January 2026. This work was supported in part by the National Key R&D Program of China under Grant 2023YFF1205200, in part by the Shenzhen Medical Research Fund under Grant B2502031, in part by the National Natural Science Foundation of China under Grant 62222318, Grant 62273173, and Grant 62373010, in part by the Guangdong Major Project of Basic Research under Grant 2025B0303000003, in part by the Shenzhen Science and Technology Program under Grant JCYJ20240813094403005, and in part by the Research Grants Council of the Hong Kong Special Administrative Region of China under Project CityU/11210424. This article was recommended for publication by Associate Editor Elena D. Momi and Editor M. Schwager upon evaluation of the reviewers' comments. *(Corresponding author: Mingming Zhang.)*

Cui Wang is with the Department of Biomedical Engineering, Southern University of Science and Technology, Shenzhen 518055, China, and also with the Department of Mechanical Engineering, City University of Hong Kong, Hong Kong, China (e-mail: 12250105@mail.sustech.edu.cn).

Yudong Liu, Chenyang Sun, Yi-Feng Chen, and Mingming Zhang are with the Shenzhen Key Laboratory of Smart Healthcare Engineering, Department of Biomedical Engineering, Southern University of Science and Technology, Shenzhen 518055, China (e-mail: 12132635@mail.sustech.edu.cn; 12131149@mail.sustech.edu.cn; chenyf6@sustech.edu.cn; zhangmm@sustech.edu.cn).

Ping Li is with the School of System Design and Intelligent Manufacturing, Southern University of Science and Technology, Shenzhen 518055, China (e-mail: lip3@sustech.edu.cn).

Mingjie Dong is with the College of Mechanical and Energy Engineering, Beijing University of Technology, Beijing 100124, China (e-mail: dongmj@bjut.edu.cn).

Zhenhong Li is with the School of Engineering, University of Manchester, 100124 Manchester, U.K. (e-mail: zhenhong.li@manchester.ac.uk).

Lu Liu is with the Department of Mechanical Engineering, City University of Hong Kong, Hong Kong, SAR, China (e-mail: luliu45@cityu.edu.hk).

This article has supplementary downloadable material available at https://doi.org/10.1109/TRO.2026.3651680, provided by the authors.

Digital Object Identifier 10.1109/TRO.2026.3651680

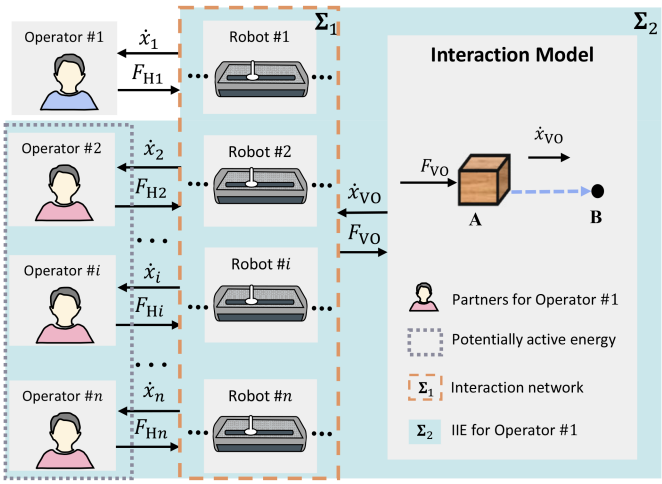

Fig. 1. Collaborative manipulation using M-Hers: A team of human operators are tasked to move a common virtual object, where the partners might inject active energy into human operators' IIE. $\dot{x}_i$ and $F_{\mathrm{H}i}$ denote the velocity and interaction forces of *Operator #i*, respectively. F_{VO} and x_{VO} are the force input and velocity output of the interaction model, respectively. The M-Hers consists of an $(n+1)$-port network Σ_1, n human operators and an interaction model that achieved through virtual environment. Here, the $(n+1)$-port network is referred to as interaction network.

(e.g., the $(n+1)$-port network Σ_1 in Fig. 1) is passive. However, in various scenarios, nonpassive human behaviors are essentially for performing voluntary tasks, rendering this paradigm invalid.

In M-Hers where nonpassive terminations (e.g., environments or human operators) are present, control design often relies on the passivity/activity degree of these terminations (e.g., excess or shortage of passivity). Existing approaches can be broadly classified into two categories: 1) constructing augmented interaction network that incorporates the passivity/activity degree of all terminations [7]. However, as the number of terminations increases, the dimension of the immittance matrix for the new network expands, making the network's stability conditions more complex and complicating the determination of controller gains necessary to ensure stability. 2) Designing a controller that synthesizes passivity degree of the passive termination [8]. This approach focuses on modulating the force transmission path between a nonpassive termination and a passive termination, typically by scaling forces based on the passivity degree of the latter [8]. However, this approach assumes a single force transmission path, which is infeasible in systems with multiple terminations. As the number of terminations grows, multiple coupled force transmission paths emerge, making accurate modulation among passive and nonpassive terminations impractical. Both methods face scalability limitations, underscoring the need for more robust strategies to handle complex interactions in M-Hers with numerous terminations.

To address these scalability challenges in M-Hers with nonpassive terminations, this work proposes an augmented tank-based control framework that consists two steps. First, to improve scalability, we introduce the concept of the individual interaction environment (IIE), which enables independent controller design within each human–robot subsystem. This step mitigates the effects of complex stability requirements (e.g., intricate stability conditions) and interaction coupling. The IIE serves as a workspace that captures each operator's task perception, integrating both virtual object and partner-induced effects (see Σ_2 in Fig. 1). Second, within each operator's IIE, passivity violations caused by active partners' behaviors are identified and addressed using an augmented tank-based controller (ATBC), ensuring that nonpassive actions are executed in a passive manner. In our collaborative virtual environment, as shown in Fig. 2, forces exerted by all operators influence the motion of a shared virtual object. Operators perceive altered task dynamics, such as easier object mobility with increased partner forces or harder mobility with decreased or opposing partners' forces. These dynamics are directly influenced by the energy injected into or extracted from the IIE by the partners. By isolating passivity violations within each workspace, the IIE facilitates controller design that maintains passive IIE while preserving haptic transparency.

A. Related Work

1) Methods Assuming Passive Terminations: As previously discussed, ensuring the passivity of the interaction network is essential to guarantee the overall stability of M-Hers, provided that all terminations are passive. One strategy to maintain a passive interaction network extends Raisbeck's passivity criterion from 2-port networks to n-port ones. The work in [9] first introduced $2n$ conditions on immittance matrix and their residues at the imaginary-axis poles to ensure passivity for n-port networks. This criterion has been applied to dual-user [10], [11] and triple-user haptic systems [12], with simulation or experimental validation demonstrating its practicality for controller design. However, this approach relies on constructing immittance matrices, which requires the system to be either linear or can be linearized. In addition, as the number of terminations increases, the complexity of immittance matrix and the associated passivity conditions grows, making the approach increasingly challenging to implement.

Alternative approaches, such as wave-based control and TDPA can alleviate these limitations on system model and the number of terminations. Studies [13], [14] utilized a wave node to interconnect multiple wave variable transmission lines in a power-preserving way, ensuring passivity regardless of the number of terminals. However, wave-based methods suffer from intrinsic issues, such as wave reflections and position drift, which can threaten system stability. In [15] and [16], track-TDPA was developed to ensure passivity in delayed tracks and subsystems by assuming passive agents; thereby ensuring overall system passivity. In [17] and [18], a multilateral system was decoupled into subsystems with respect to each conjugate power pair, with TDPA deployed to passify each subsystem. In summary, TDPA approach relies on the fundamental property that the passivity of each component in a network ensures stability of the overall network system.

2) Methods Considering Nonpassive Terminations: Llewellyn's absolute stability criterion has been used for stability analysis of M-Hers with nonpassive terminations. For example, the works in [2] and [19] extended Llewellyn's criterion to bilateral systems involving nonpassive operators or environments by using Möbius transformations to map termination impedance to driving-point impedance. However, this approach is limited to 2-port networks. The work in [7] addressed this limitation by applying series-shunt decomposition to each termination impedance via Möbius transformation, where an augmented network immittance matrix was constructed and then analyzed using Llewellyn's

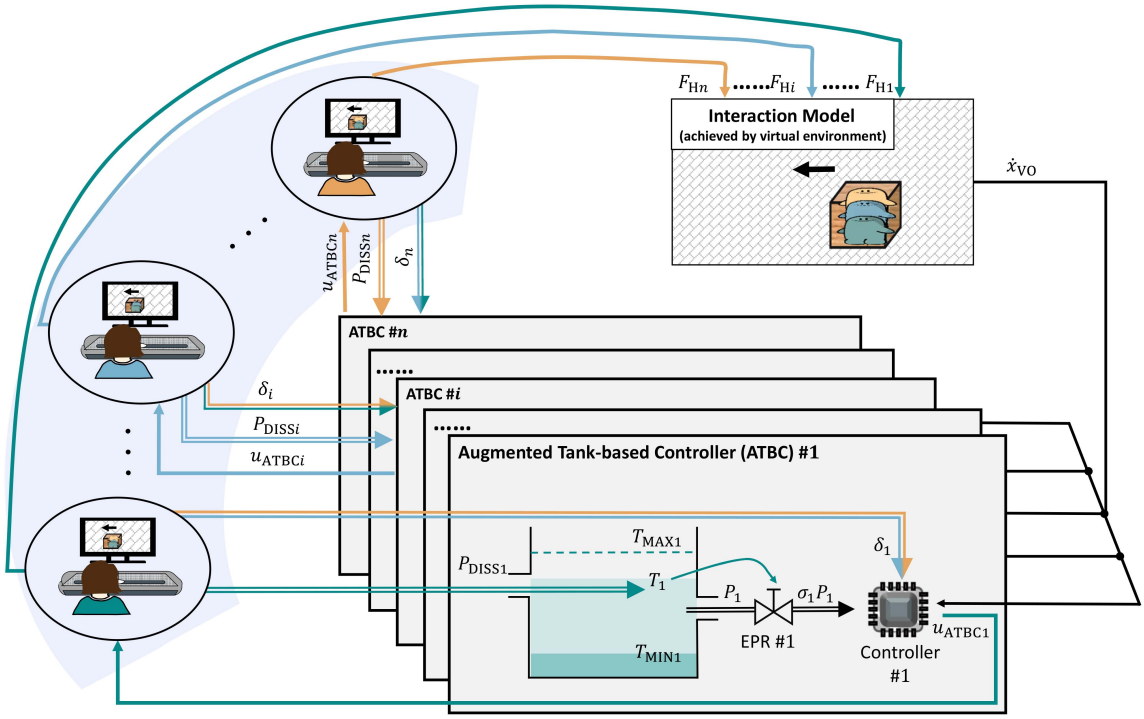

Fig. 2. Architecture of the collaborative manipulation using M-Hers with ATBC. EPR denotes energy-related power regulation. The definition of δ_i, $P_{\mathrm{DISS}i}$, σ_i, and $u_{\mathrm{ATBC}i}$ is defined as (11), (12), (26), and (30), respectively.

absolute stability criterion. However, this method faces two primary limitations that hinder scalability. First, as the number of terminations increases, the stability conditions for the augmented immittance matrix become increasingly complex, complicating the determination of control gains. Second, the method relies on known boundaries for the real part of the nonpassive termination impedance, which is difficult to determine in practice due to variations among operators or environments.

Passivity analysis that considers the impact of partners' behaviors has been explored in bilateral haptics-enabled telerobotic rehabilitation. This scenario allows a therapist to fully supervise rehabilitation procedures by delivering resistive or assistive motor therapy. The work in [8] proposed integrating human biomechanical capabilities (i.e., excess of passivity) into controller design to address active interaction energy and guarantee safe patient–robot interaction during assistive therapies. This method provided patients with a passive interaction environment while delivering nonpassive assistance and has been further explored in [20], [21], [22], and [23]. However, these approaches are limited to bilateral systems, as discussed earlier.

3) Energy Tank: Energy tanks have been extensively used to guarantee system passivity in various contexts, including robot manipulation [24], human–robot interaction systems with variable impedance/admittance [25], [26], multirobot systems with time-varying potential fields [27], time-varying topologies [28], [29], and redundant manipulators implementing hierarchical tasks [30], [31]. Power regulation has often been integrated into energy tanks to enhance controller safety by scaling down nonpassive control actions and regulating the rate of energy exchange between the controller and the energy tank. For instance, the studies in [32], [33], and [34] augmented energy tanks with constant power regulation (CPR). However, these methods can be sensitive to inappropriate power limits. Excessively high-power bounds may render power regulation ineffective due to the rapid release and potential depletion of tank energy, while overly restrictive bounds can compromise control objectives by scaling down the desired nonpassive behaviors. To alleviate this, studies have proposed methods, such as iterative learning [35], optimization algorithm [31], and adaptive control [36], to determine appropriate power bounds. However, these methods often incur significant computation costs, which can limit their practicality. Consequently, a straightforward and computationally efficient power regulation approach with flexible power bound remains critically important for ensuring passivity and achieving robust control performance.

B. Contribution and Organization

This work focuses on passifying IIE in M-Hers involving at least three human operators, without assuming the operators are passive. Unlike previous methods based on termination impedance [2], [7], [19], our approach introduces the concept of IIE and analyzes its interconnection with the human hand, emphasizing the force feedback mechanisms between the operator's hand and the IIE. This analysis simplifies the controller design by eliminating the need for termination impedance and directly utilizing force data measured by force sensors. Furthermore, the introduction of the IIE facilitates the passivity analysis of the overall system by isolating and passifying each operator's workspace individually, thereby enhancing the scalability of the control framework. In contrast to traditional termination impedance-based methods, our approach provides a more efficient solution for complex multiuser

environments characterized by highly dynamic and coupled interactions.

Based on the above human-IIE interconnection analysis, we identify passivity-violating components resulting from the nonpassive partners' behaviors within the IIE and propose an ATBC to ensure IIE passivity while maintaining realistic multiuser haptic interaction. The ATBC employs power regulation to prevent tank energy depletion, which could otherwise cause unstable system behaviors when the tank energy reaches its minimum allowable value. Our method only scales the nonpassive power flows while compensating for the resultant nonpassivity and its effects on rendering accuracy, distinguishing it from existing methods that scale both the nonpassive control actions and power flows [31], [32], [33], [34], [35]. This approach helps avoid the degradation of key task objectives directly caused by power regulation (e.g., modifications to the desired trajectory/force and degradation of force regulation), a challenge that has rarely been addressed in the literature. The main contributions of this work are summarized as follows.

1) In the IIE framework, we theoretically demonstrate that partners' active behaviors, such as introducing variable impedance/admittance-type IIEs or providing assistance, can compromise IIE passivity. We also identify potential passivity-violating components and address them within each operator's IIE. This framework facilitates both independent passivity analysis and controller design for each human–robot subsystem, thereby enhancing scalability. To the best of authors' knowledge, this is the first exploration of IIE passivity in the context of M-Hers.
2) To address the impacts of nonpassive human behaviors on IIE passivity, we propose a novel ATBC method integrating an energy-related power regulation (EPR) scheme and a time-varying control gain. The EPR scheme intuitively determines the power bound from real-time available tank energy, which prevents tank energy depletion under larger power bounds and facilitates practical implementation by improving computational efficiency and ensuring robustness across various power settings relative to the CPR scheme. Meanwhile, the time-varying control gain mitigates the negative effects of power regulation on rendering accuracy, even with a smaller power bound. This dual innovation achieves a favorable balance between passivity and rendering fidelity, as validated through theoretical analysis and extensive experiments.

The rest of this article is organized as follows. In Section II, we introduce preliminaries and problem formulation. Section III describes the interconnection structure of the overall system and identifies passivity-violating components within each operator's IIE. Section IV develops a tank-based controller (TBC) to address the presented problem and augments it with an EPR scheme. Section V analyzes the convergence of the closed-loop system. In Section VI, experiments have been carried out using a customized M-Hers to validate the proposed controller. Finally, Section VII concludes this article.

II. Preliminaries and Problem Formulation

This section begins by introducing the robotic dynamics and interaction model, which form the foundation of analyzing M-Hers. Then, two propositions are presented to examine the impacts of partners' behaviors on the IIE. Finally, the problem addressed in this work is articulated in detail.

A. Robotic Dynamics

In M-Hers, the dynamic model of the ith robot in m-dimensional Cartesian space is given by

$$D_i(x_i)\ddot{x}_i + C_i(x_i,\dot{x}_i)\dot{x}_i + G_i(x_i) = u_i + F_{\mathrm{H}i} \quad i = 1,2,\ldots,n \tag{1}$$

where $x_i \in \mathbb{R}^m$ is the pose of the end-effector, $D_i(x_i) \in \mathbb{R}^{m\times m}$ is the symmetric positive-definite inertia matrix, $C_i(x_i,\dot{x}_i) \in \mathbb{R}^{m\times m}$ represents the Coriolis and centrifugal forces, $G_i(x_i) \in \mathbb{R}^m$ is the gravity vector, $u_i \in \mathbb{R}^m$ is the control input, and $F_{\mathrm{H}i} \in \mathbb{R}^m$ is the interaction force exerted by the ith human operator and measured by the force/torque sensor mounted on the end-effector.

B. Interaction Model

The interaction model is implemented through virtual environment, as shown in Fig. 2. The virtual object model is defined as follows:

$$M_{\mathrm{VO}}\ddot{x}_{\mathrm{VO}} + B_{\mathrm{VO}}\dot{x}_{\mathrm{VO}} = F_{\mathrm{VO}} \tag{2}$$

where $M_{\mathrm{VO}} \in \mathbb{R}^{m\times m}$ and $B_{\mathrm{VO}} \in \mathbb{R}^{m\times m}$ denote the mass and damping of the virtual object, respectively; $F_{\mathrm{VO}} = \sum_{i=1}^{n} F_{\mathrm{H}i} \in \mathbb{R}^m$ is the total force exerted to the virtual object, $\ddot{x}_{\mathrm{VO}}, \dot{x}_{\mathrm{VO}} \in \mathbb{R}^m$, respectively, represent the acceleration and velocity of the virtual object, and x_{VO} is the position of the virtual object, which is also the reference command for each robot and human hand.

C. Problem Definition

In this part, two propositions are introduced to validate the existence of the problem addressed in this work, which focus on the impacts of partners' behavior on IIE, as illustrated in Fig. 1. Then, the problem is formalized.

Proposition 1: In M-Hers, partners' behaviors cause variable impedance/admittance characteristics for the IIE.

Proof: See Appendix A. ■

Proposition 2: In M-Hers, partners' behaviors that act as a form of assistance may violate the IIE passivity condition.

Proof: See Appendix B. ■

Remark 1: Existing studies have extensively explored that variable impedance/admittance models are potentially nonpassive due to changes stiffness or inertial terms [37], [38]. Furthermore, research in bilateral telerobotic rehabilitation has verified that assistance from the therapists can lead to a nonpassive interaction environment for the patient [20], [22], [39]. The above propositions point out that partners' behaviors primarily affect the IIE through two main mechanisms: 1) the introduction of variable impedance/admittance and 2) assistance behaviors, both of which violate the passivity condition. However, in M-Hers, accurately modeling the IIE and the specific assistance provided by partners is almost impossible due to the interaction coupling in the interaction model.

Problem 1: Consider the M-Hers described by the robotic dynamics (1) and the interaction model (2) with nonpassive human operators. Develop a TBC $u_{\mathrm{TBC}i}$ such that the IIE for *Operator #i* is passive with respect to $(F_{\mathrm{H}i}, \dot{x}_i)$, that is, $\dot{V}_{\mathrm{TBC}i} \le \dot{x}_i^T F_{\mathrm{H}i}$ with $V_{\mathrm{TBC}i}$ being the total storage energy in IIE under $u_{\mathrm{TBC}i}$.

Problem 2: Given the solution to the Problem 1, further consider the power regulation to enhance controller safety and its impacts on rendering fidelity. Develop an ATBC $u_{\mathrm{ATBC}i}$ such that the following properties hold.

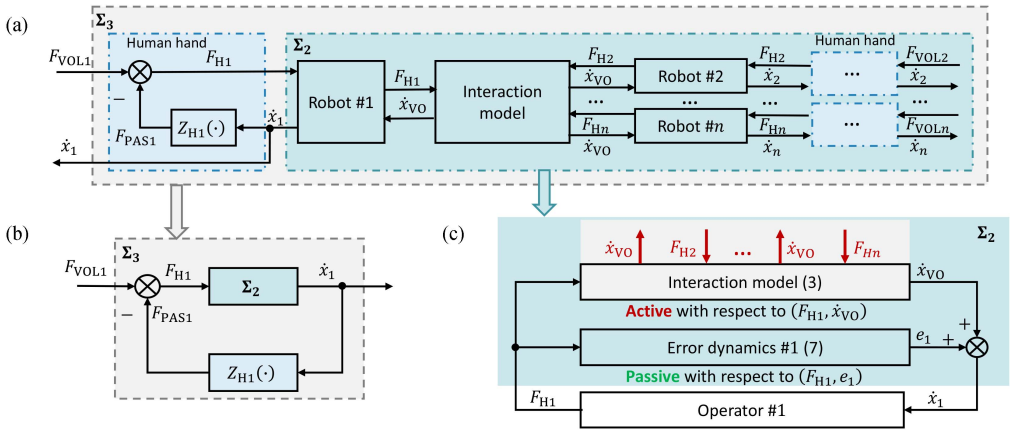

Fig. 3. (a) Illustration of the IIE for *Operator #*1. (b) Feedback interconnection of Σ_2 and Z_{H1} in Σ_3. (c) Parallel interconnection of interaction model and error dynamics in Σ_2 under classical controller (5). Σ_2 is the practical IIE, Σ_3 is the theoretical IIE and $Z_{H1}(\cdot) = Z_{H1}(t, \dot{x}_1)$.

1) The IIE for *Operator #i* is passive with respect to $(F_{Hi}, \dot{x}_i)$, that is, $\dot{V}_{ATBCi} \leq \dot{x}_i^T F_{Hi}$ with V_{ATBCi} being the total storage energy in IIE under u_{ATBCi}.
2) The velocity tracking error $e_i = \dot{x}_i - \dot{x}_{VO}$ is bounded.
3) The EPR-induced part of the error is addressed by the time-varying control gain.

To address the above problems, the following properties of robot dynamics and assumptions are outlined as follows.

Property 1 (see[40]): The skew-symmetric matrix $2C_i(x_i, \dot{x}_i) - \dot{D}_i(x_i)$ satisfies that

$$\xi^T \left(2C_i(x_i, \dot{x}_i) - \dot{D}_i(x_i)\right) \xi = 0 \quad \forall \xi \in \mathbb{R}^m.$$

Property 2 (see[41]): The dynamic model described by (1) has the property of linear parameterization. For all differentiable vector $\chi_i \in \mathbb{R}^m$

$$D_i(x_i)\dot{\chi}_i + C_i(x_i, \dot{x}_i)\chi_i + G_i(x_i) = Y_i(x_i, \dot{x}_i, \chi_i, \dot{\chi}_i)\theta_i$$

where $Y_i(x_i, \dot{x}_i, \chi_i, \dot{\chi}_i) \in \mathbb{R}^{m \times p}$ is a known regression matrix, and $\theta_i \in \mathbb{R}^p$ is the constant parameter vector of *Robot #i*. In this work, χ_i and $\dot{\chi}_i$ denote the reference end-effector velocity $\dot{x}_{VO}$ and end-effector acceleration $\ddot{x}_{VO}$, respectively.

Assumption 1: The human interaction force $F_{Hi}(i = 1, 2, \ldots, n)$ is bounded during the interaction task [20]. The position of the virtual object x_{VO} is also bounded.

Assumption 2: The interaction force $F_{Hi}(i = 1, 2, \ldots, n)$ contains both voluntary and passive components, i.e., $F_{Hi} = F_{VOLi} - F_{PASi}$, where F_{VOLi} represents the exogenous independent voluntary component, which can generate nonpassive energy for the IIE. $F_{PASi} = Z_{Hi}(t, \dot{x}_i)$ denotes the passive component, which is a nonlinear impedance model [42].

In Assumption 1, it is practical to assume the bounded human forces in the context of human–robot interaction. The similar assumptions have been adopted in [6], that is, human forces are assumed to have bounded energy. In Assumption 2, the passive component F_{PAS1} can be nonlinear, which relaxes the conventional linearity assumption on human upper limb, such as in [43], [44], and [45].

III. Identification of Passivity-Violating Components Within IIE

In M-Hers, human operators interact by manipulating the virtual object, as illustrated in Fig. 3(a). According to Assumption 2, the theoretical IIE that each operator interacts with is denoted as Σ_3, where the active component F_{VOLi} is difficult to obtain accurately in practice. However, due to the passive component F_{PAS1} and the feedback interconnection between $Z_{H1}(\bullet)$ and Σ_2, as shown in Fig. 3(b), the passivity of Σ_2 implies the passivity of Σ_3 (A proof can be seen in Appendix C). Therefore, the controller design in this work focuses on ensuring the passivity of the practical IIE Σ_2, which is potentially nonpassive due to partners' behaviors as illustrated in Fig. 3(c).

To achieve collaborative haptic interaction, the human operators' motion is expected to remain consistent with the virtual object. Assuming stiff contact between human operators' hands and robots, the control goal can be stated as enabling the robots' motion to track the virtual object's motion while ensuring a passive IIE. In this context, velocity tracking performance serves as a measure of rendering accuracy.

The velocity tracking error between *Robot #i* and the virtual object is defined as

$$e_i = \dot{x}_i - \dot{x}_{VO}, \ i = 1, 2, \ldots, n. \tag{3}$$

From Property 2, there exists a known matrix $Y_{di}(x_i, \dot{x}_i, \dot{x}_{VO}, \ddot{x}_{VO})$ and an unknown constant vector θ_i such that

$$Y_{di}(x_i, \dot{x}_i, \dot{x}_{VO}, \ddot{x}_{VO})\theta_i = D_i(x_i)\ddot{x}_{VO} + C_i(x_i, \dot{x}_i)\dot{x}_{VO} + G_i(x_i) \tag{4}$$

where $D_i(x_i)$, $C_i(x_i, \dot{x}_i)$, and $G_i(x_i)$ are the robot dynamics terms as defined in (1). Without considering the requirement of ensuring a passive IIE, the robot controller u_i can be formulated as the following basic velocity tracking controller [46] to render the multiuser haptic interaction environment.

$$u_{BASEi} = -K_{Pi}e_i - K_{Ii}E_i + Y_{di}\left(x_i, \dot{x}_i, \dot{x}_{VO}, \ddot{x}_{VO}\right)\hat{\theta}_i \tag{5}$$

with

$$\dot{\hat{\theta}}_i = -\Lambda_i Y_{di}^T\left(x_i, \dot{x}_i, \dot{x}_{VO}, \ddot{x}_{VO}\right) e_i \tag{6}$$

where K_{Pi}, K_{Ii}, and Λ_i are the designed positive definite diagonal matrices, $E_i = \int e_i dt$ is the integral of the tracking error,

$\hat{\theta}_i = \theta_i - \widetilde{\theta}_i$ is the estimated vector, and $\widetilde{\theta}_i$ is the estimation error. In this section, the control input $u_i = u_{\mathrm{BASE}i}$.

Substituting (3)–(6) into (1), the error dynamics can be derived as

$$D_i(x_i)\dot{e}_i + C_i(x_i,\dot{x}_i)e_i + Y_{\mathrm{d}i}(x_i,\dot{x}_i,\dot{x}_{\mathrm{VO}},\ddot{x}_{\mathrm{VO}})\widetilde{\theta}_i = -K_{\mathrm{P}i}e_i - K_{\mathrm{I}i}E_i + F_{\mathrm{H}i}. \tag{7}$$

From Fig. 3(c), the IIE includes closed-loop system and interaction model. For the ith closed-loop system (7), its storage function is expressed as

$$V_{\mathrm{CL}i} = \frac{1}{2}e_i^T D_i(x_i)e_i + \frac{1}{2}E_i^T K_{\mathrm{I}i}E_i + \frac{1}{2}\widetilde{\theta}_i^T\Lambda_i^{-1}\widetilde{\theta}_i. \tag{8}$$

Taking the derivative of (8) and substituting (6) and (7), while using Property 1, yields

$$\begin{aligned}\dot{V}_{\mathrm{CL}i} &= e_i^T D_i(x_i)\dot{e}_i + \frac{1}{2}e_i^T\dot{D}_i(x_i)e_i \\ &\quad + e_i^T K_{\mathrm{I}i}E_i - \widetilde{\theta}_i^T\Lambda_i^{-1}\dot{\hat{\theta}}_i \\ &= e_i^T D_i(x_i)\dot{e}_i + \frac{1}{2}e_i^T\dot{D}_i e_i + e_i^T\Big(-K_{\mathrm{P}i}e_i \\ &\quad + F_{\mathrm{H}i} - D_i(x_i)\dot{e}_i - C_i(x_i,\dot{x}_i)e_i \\ &\quad - Y_{\mathrm{d}i}(x_i,\dot{x}_i,\dot{x}_{\mathrm{VO}},\ddot{x}_{\mathrm{VO}})\widetilde{\theta}_i\Big) \\ &\quad + \widetilde{\theta}_i^T Y_{\mathrm{d}i}^T(x_i,\dot{x}_i,\dot{x}_{\mathrm{VO}},\ddot{x}_{\mathrm{VO}})e_i \\ &= e_i^T F_{\mathrm{H}i} - e_i^T K_{\mathrm{P}i}e_i.\end{aligned} \tag{9}$$

In addition, the stored energy of the interaction model is defined as $S_{\mathrm{VO}} = \frac{1}{2}\dot{x}_{\mathrm{VO}}^T M_{\mathrm{VO}}\dot{x}_{\mathrm{VO}}$. Using (2), its derivative is computed as

$$\dot{S}_{\mathrm{VO}} = \dot{x}_{\mathrm{VO}}^T F_{\mathrm{VO}} - \dot{x}_{\mathrm{VO}}^T B_{\mathrm{VO}}\dot{x}_{\mathrm{VO}}. \tag{10}$$

Therefore, the total stored energy of the IIE is defined as $V_{\mathrm{IIE}i} = V_{\mathrm{CL}i} + S_{\mathrm{VO}}$. Taking its derivative and invoking (3), (9), and (10), we obtain

$$\begin{aligned}\dot{V}_{\mathrm{IIE}i} &= \dot{x}_i^T F_{\mathrm{H}i} - e_i^T K_{\mathrm{P}i}e_i - \dot{x}_{\mathrm{VO}}^T F_{\mathrm{H}i} + \dot{x}_{\mathrm{VO}}^T F_{\mathrm{VO}} \\ &\quad - \dot{x}_{\mathrm{VO}}^T B_{\mathrm{VO}}\dot{x}_{\mathrm{VO}} \\ &= \dot{x}_i^T F_{\mathrm{H}i} - e_i^T K_{\mathrm{P}i}e_i - \dot{x}_{\mathrm{VO}}^T B_{\mathrm{VO}}\dot{x}_{\mathrm{VO}} \\ &\quad + \underbrace{\dot{x}_{\mathrm{VO}}^T\sum_{k=1}^{n}F_{\mathrm{H}k}}_{\delta_i}\end{aligned} \tag{11}$$

where $k = 1, 2, \ldots, n$ and $k \neq i$. Obviously, δ_i is the potentially passivity-violating component. This term can be positive if the partners introduce energy into IIE, which implies that the IIE for *Operator #i* can be active with respect to the input–output pair $(F_{\mathrm{H}i}, \dot{x}_i)$.

IV. ATBC Design

To preserve the passivity of IIE, the concept of an energy tank is adopted to develop a TBC, enabling the passivity-violating components to be implemented in a passive manner. However, maintaining IIE passivity remains a challenge, especially under aggressive behaviors, such as increased force inputs from partners, which can accelerate energy release from the tank and potentially deplete its energy. To mitigate these risks, we augment the TBC with a novel EPR scheme to regulate the rate of energy exchange between the tank and the controller within specified constraints, ensuring the tank energy remains above a minimum threshold. The proposed control scheme is illustrated in Fig. 4.

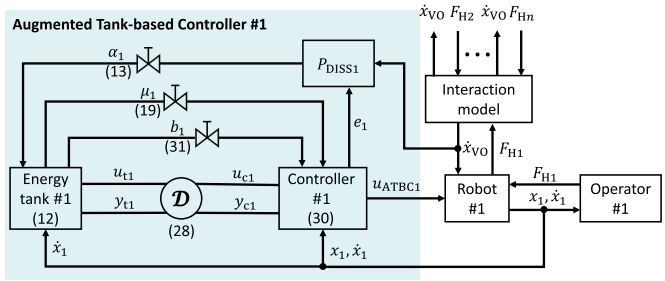

Fig. 4. Overview of the control framework for *Operator #1*.

A. Tank-Based Controller

We define an energy tank with the state $x_{\mathrm{t}i} \in \mathbb{R}$ and the storage function $T_i(x_{\mathrm{t}i}) = \frac{1}{2}x_{\mathrm{t}i}^2$. In the analysis, $T_i(x_{\mathrm{t}i})$ will be abbreviated as T_i. The tank dynamics is defined as

$$\dot{x}_{\mathrm{t}i} = \frac{\alpha_i}{x_{\mathrm{t}i}}P_{\mathrm{DISS}i} + u_{\mathrm{t}i} \tag{12}$$

where $P_{\mathrm{DISS}i} = e_i^T K_{\mathrm{P}i}e_i + \dot{x}_{\mathrm{VO}}^T B_{\mathrm{VO}}\dot{x}_{\mathrm{VO}} - \gamma_i\delta_i$ denotes the rate of dissipated energy in the subsystem #i, $u_{\mathrm{t}i}$ represents the tank input, α_i enables or disables the injection of energy into the tank to prevent the tank energy from exceeding the maximum value $T_{\mathrm{MAX}i}$. It is defined as

$$\alpha_i = \begin{cases} c_i, & \text{if } T_i < T_{\mathrm{MAX}i} \\ 0, & \text{otherwise} \end{cases} \tag{13}$$

where $0 < c_i < 1$ is a positive constant to be designed. In this work, c_i is set to be smaller than one due to energy conservation, and further satisfies $\sum_{i=1}^{n} c_i = 1$. The variable γ_i accounts for monitoring the potentially passivity-violating components δ_i and is defined as

$$\gamma_i = \begin{cases} 1, & \text{if } \delta_i \leq 0 \\ 0, & \text{otherwise} \end{cases} \tag{14}$$

which enables/disables the injection of energy into the tank due to δ_i. Based on (12), when $\gamma_i = 1$, the variable δ_i serves as a dissipation term and its associated energy will be injected to the energy tank. In contrast, when $\gamma_i = 0$, the energy injection is stopped and the energy extraction is instead necessary to compensate for the nonpassivity behaviors. This is achieved by the following interconnection between energy tank and the controller through the power ports $(u_{\mathrm{t}i}, y_{\mathrm{t}i})$ and $(u_{\mathrm{c}i}, y_{\mathrm{c}i})$ in the following power-preserving manner:

$$\begin{bmatrix} u_{\mathrm{c}i} \\ u_{\mathrm{t}i} \end{bmatrix} = \begin{bmatrix} 0 & \omega_i \\ -\omega_i^T & 0 \end{bmatrix}\begin{bmatrix} y_{\mathrm{c}i} \\ y_{\mathrm{t}i} \end{bmatrix} \tag{15}$$

with $y_{\mathrm{c}i} = \dot{x}_i$ and $y_{\mathrm{t}i} = x_{\mathrm{t}i}$. ω_i denoting the interconnection between tank and controller, which is defined by

$$\omega_i = \beta_i(1-\gamma_i)\frac{\sum_{k=1}^{n}F_{\mathrm{H}k}}{x_{\mathrm{t}i}} \tag{16}$$

where the variable γ_i is responsible for the activation of energy extraction when the potential nonpassivity is detected, and the

variable β_i is deployed as

$$\beta_i = \begin{cases} 1, & \text{if } T_i \geq T_{\text{MIN}i} \\ 0, & \text{otherwise} \end{cases} \tag{17}$$

where $T_{\text{MIN}i}$ is the lower limit of energy tank, which should be greater than zero to avoid singularity in (12), i.e., $T_{\text{MIN}i} > 0$. $\beta_i = 1$ indicates available tank energy tank to compensate for the nonpassive behavior, and $\beta_i = 0$ means that the tank is depleted and detached from the controller. However, this detachment may compromise IIE passivity if the potential passivity-violating component δ_i remains positive. To address this issue, we modify the robot controller u_i to the following TBC based on controller $u_{\text{BASE}i}$ in (5), as follows:

$$u_{\text{TBC}i} = u_{\text{BASE}i} + u_{ci} - \alpha_i \mu_i e_i \tag{18}$$

where u_{ci} is the controller input due to the interconnection with energy tank, which is defined in (15), and μ_i is a variable damper, which is given by

$$\mu_i = \begin{cases} \frac{\delta_i}{\alpha_i e_i^T e_i}, & \text{if } \gamma_i = 0 \text{ and } \beta_i = 0 \\ 0, & \text{otherwise} \end{cases} \tag{19}$$

indicating that μ_i is activated under the conditions of both potential nonpassivity and tank energy depletion.

The strategy described above guarantees IIE passivity, as proven in the following theorem.

Theorem 1: Under Assumptions 1 and 2, the problem of ensuring IIE passivity in M-Hers involving nonpassive human operators, as defined in Problem 1, is solved by the TBC $u_{\text{TBC}i}$ (18) based on the energy tank (12).

Proof: The total storage energy in IIE under TBC (18) is defined as $V_{\text{TBC}i} = V_{\text{IIE}i} + T_i$, where $V_{\text{IIE}i}$ is detailed in (11).

Substituting (18) into (1), the error dynamics can be obtained as

$$\begin{aligned} &D_i(x_i)\dot{e}_i + C_i(x_i, \dot{x}_i)e_i + Y_{\text{d}i}(x_i, \dot{x}_i, \dot{x}_{\text{VO}}, \ddot{x}_{\text{VO}})\widetilde{\theta}_i \\ &= -K_{\text{I}i}E_i - K_{\text{P}i}e_i + F_{\text{H}i} + \beta_i(1-\gamma_i)\sum_{k=1}^{n} F_{\text{H}k} - \alpha_i\mu_i e_i. \end{aligned} \tag{20}$$

Taking the derivative of $V_{\text{IIE}i}$ and invoking (18), we have

$$\begin{aligned} \dot{V}_{\text{IIE}i} &= \dot{x}_i^T F_{\text{H}i} - e_i^T K_{\text{P}i} e_i - \dot{x}_{\text{VO}}^T B_{\text{VO}} \dot{x}_{\text{VO}} + \delta_i \\ &\quad + \beta_i(1-\gamma_i) e_i^T \sum_{k=1}^{n} F_{\text{H}k} - \alpha_i \mu_i e_i^T e_i. \end{aligned} \tag{21}$$

From (12) and (15), the derivative of T_i is given by

$$\begin{aligned} \dot{T}_i &= \alpha_i \left(e_i^T K_{\text{P}i} e_i + \dot{x}_{\text{VO}}^T B_{\text{VO}} \dot{x}_{\text{VO}} - \gamma_i \delta_i \right) \\ &\quad - \beta_i(1-\gamma_i)\dot{x}_i^T \sum_{k=1}^{n} F_{\text{H}k}. \end{aligned} \tag{22}$$

From (21) and (22), the derivative of $V_{\text{TBC}i}$ is derived as

$$\begin{aligned} \dot{V}_{\text{TBC}i} &= \dot{x}_i^T F_{\text{H}i} - (1-\alpha_i) e_i^T K_{\text{P}i} e_i \\ &\quad - (1-\alpha_i)\dot{x}_{\text{VO}}^T B_{\text{VO}} \dot{x}_{\text{VO}} \\ &\quad + (1 - \alpha_i\gamma_i)\delta_i - \beta_i(1-\gamma_i)\delta_i - \alpha_i\mu_i e_i^T e_i \\ &\leq \dot{x}_i^T F_{\text{H}i} - (1-\alpha_i) e_i^T K_{\text{P}i} e_i \\ &\quad + (1 - \gamma_i(\alpha_i - \beta_i) - \beta_i)\delta_i - \alpha_i\mu_i e_i^T e_i. \end{aligned} \tag{23}$$

The "$\leq$" results from (13), which implies that $(1-\alpha_i)\dot{x}_{\text{VO}}^T B_{\text{VO}} \dot{x}_{\text{VO}} \geq 0$. Given that $\alpha_i \in (0,1)$ and $e_i^T K_{\text{P}i} e_i \geq 0$, it follows that

$$\dot{x}_i^T F_{\text{H}i} \geq \dot{V}_{\text{TBC}i} - (1 - \gamma_i(\alpha_i - \beta_i) - \beta_i)\delta_i + \alpha_i\mu_i e_i^T e_i. \tag{24}$$

If $\gamma_i = 1$, then $\mu_i = 0$. From (24), it obtains

$$\dot{x}_i^T F_{\text{H}i} \geq \dot{V}_{\text{TBC}i} - (1-\alpha_i)\delta_i \geq \dot{V}_{\text{TBC}i}. \tag{25}$$

If $\gamma_i = 0$, two scenarios arise. First, if $\beta_i = 1$, implying that $\mu_i = 0$, then (24) becomes $\dot{x}_i^T F_{\text{H}i} \geq \dot{V}_{\text{TBC}i}$. This indicates that the desired nonpassive behaviors can be implemented in a passive manner as long as the tank energy remains above the threshold $T_{\text{MIN}i}$. Second, if $\beta_i = 0$, implying that $\alpha_i\mu_i\dot{e}_i^T\dot{e}_i = \delta_i$, then (24) becomes $\dot{x}_i^T F_{\text{H}i} \geq \dot{V}_{\text{TBC}i}$. In this case, the energy tank detaches from the controller, and the variable damper μ_i is simultaneously activated to dissipate the additional energy generated by the partners' active behaviors, thereby ensuring the passivity of IIE. Therefore, it can be concluded that the IIE for *Operator #i* is passive with respect to $(F_{\text{H}i},\ \dot{x}_i)$. ■

B. Augmented TBC

While the presented TBC theoretically preserves IIE passivity, tank depletion may occur under aggressive operator actions, as demonstrated in Sections VI-E and VI-F. This highlights the need to enforce power flow constraint to maintain passivity in practice. However, such constraint involves a safety-performance tradeoff problem. Specifically, excessively high power limit may undermine the effectiveness of the power regulation method, whereas a conservative power limit may degrade task performance by scaling down the desired nonpassive actions. This tradeoff poses a key challenge for power limit setting in the existing literature. For instance, the CPR scheme needs to tune the fixed power bounds according to operator experience or task requirements [32], [33], whereas the optimization or learning-based method can compute appropriate trajectories but often incur high computational cost [31], [35]. To address these limitations, we propose an EPR scheme with a time-varying control gain. Unlike existing methods, EPR avoids scaling nonpassive action, and its resulting nonpassivity is addressed by the time-varying control gain, which further mitigates the negative impacts of power regulation on control performance.

The power transferred from the tank to the controller is defined as $P_i = -u_{ti}^T y_{ti}$. To enforce constraints on P_i, a scaling factor σ_i is introduced as

$$\sigma_i = \begin{cases} \frac{P_{\text{MAX}i}}{P_i}, & \text{if } P_i > P_{\text{MAX}i} \geq 0 \\ 1, & \text{otherwise} \end{cases} \tag{26}$$

where $P_{\text{MAX}i}$ is the maximum allowable power, which serves as the core of the EPR scheme. It is designed as

$$P_{\text{MAX}i} = \frac{k_{\max}}{\Delta t}(T_i - T_{\text{MIN}i}) \tag{27}$$

where Δt is the sampling time of the controlled system and $k_{\max}$ is a positive constant to be designed. In this context, $P_{\text{MAX}i}$ denotes the rate at which the available tank energy, $T_i - T_{\text{MIN}i}$, would be depleted over a time interval of $\frac{\Delta t}{k_{\max}}$. It should be noted that the EPR scheme (27) adjusts the power bound based on the tank energy T_i in real time. Therefore, the tank will not be drained as long as $\frac{\Delta t}{k_{\max}}$ is larger than the sampling time.

Through the EPR scheme (27), the interconnection between energy tank and the controller is reformulated as follows:

$$\begin{bmatrix} u_{ci} \\ u_{ti} \end{bmatrix} = \begin{bmatrix} 0 & \sigma_i\omega_i \\ -\sigma_i\omega_i^T & 0 \end{bmatrix} \begin{bmatrix} y_{ci} \\ y_{ti} \end{bmatrix}. \tag{28}$$

TABLE I
$\dot{V}_{\mathrm{ATBC}i}$ (33) UNDER DIFFERENT TANK VALUES

γ_i	β_i	$\dot{V}_{\mathrm{ATBC}i}$
$1\Rightarrow \begin{cases}\mu_i=0\\ b_i=0\end{cases}$	–	$\dot{x}_i^T F_{\mathrm{H}i} - \underbrace{W_i}_{\geq 0} + \underbrace{(1-\alpha_i)\delta_i}_{\leq 0} \leq \dot{x}_i^T F_{\mathrm{H}i}$
0	$1\Rightarrow \mu_i=0$	$\dot{x}_i^T F_{\mathrm{H}i} - \underbrace{W_i}_{\geq 0} + \underbrace{(1-\sigma_i)\delta_i - b_i e_i^T e_i}_{=0 \text{ under } \begin{cases}\sigma_i=1\Rightarrow b_i=0\\ \sigma_i=\frac{P_{\mathrm{MAX}i}}{P_i}\Rightarrow b_i=\frac{P_i-P_{\mathrm{MAX}i}}{P_i e_i^T e_i}\delta_i\end{cases}} \leq \dot{x}_i^T F_{\mathrm{H}i}$
	$0\Rightarrow \begin{cases}\mu_i=\frac{\delta_i}{\alpha_i e_i^T e_i}\\ b_i=0\end{cases}$	$\dot{x}_i^T F_{\mathrm{H}i} - \underbrace{W_i}_{\geq 0} + \underbrace{\delta_i - (\alpha_i\mu_i+b_i)e_i^T e_i}_{=0} \leq \dot{x}_i^T F_{\mathrm{H}i}$

• $\Rightarrow$ $*$ means that • implies $*$

From (28), the power transferred from the tank to the controller is modified as

$$P_i' = \sigma_i P_i \leq P_{\mathrm{MAX}i} \quad \forall t \tag{29}$$

which indicates that the EPR scheme ensures power exchange within the permitted constraints.

To address the power bound selection dilemma, we introduce a time-varying control gain in the controller design. The robot controller u_i is designed as the following ATBC by further augmenting TBC $u_{\mathrm{TBC}i}$:

$$u_{\mathrm{ATBC}i} = u_{\mathrm{BASE}i} + u_{ci} - (\alpha_i\mu_i + b_i)e_i \tag{30}$$

where $u_{\mathrm{BASE}i}$, α_i, and μ_i are defined as (5), (13), and (19), respectively; u_{ci} is obtained from (28), and b_i is a time-varying control gain introduced to compensate for the impact of bounded power flow and is defined as

$$b_i = \begin{cases} \frac{P_i - P_{\mathrm{MAX}i}}{P_i e_i^T e_i}\delta_i, & \text{if } P_i > P_{\mathrm{MAX}i} \geq 0 \\ 0, & \text{otherwise.} \end{cases} \tag{31}$$

The proof of passivity is provided as follows.

Theorem 2: Under Assumptions 1 and 2, the problem of ensuring IIE passivity in M-Hers involving nonpassive human operators, as defined in Problem 2-1), is solved by the ATBC $u_{\mathrm{ATBC}i}$ (30). The controller is augmented by the EPR scheme (27) and the time-varying control gain (31).

Proof: Substituting (30) into (1), the error dynamics is given by

$$\begin{aligned} &D_i(x_i)\dot{e}_i + C_i(x_i,\dot{x}_i)e_i + Y_{\mathrm{d}i}(x_i,\dot{x}_i,\dot{x}_{\mathrm{VO}},\ddot{x}_{\mathrm{VO}})\tilde{\theta}_i \\ &= -K_{\mathrm{I}i}E_i - K_{\mathrm{P}i}e_i + F_{\mathrm{H}i} + \beta_i(1-\gamma_i)\sigma_i\sum_{k=1}^{n}F_{\mathrm{H}k} \\ &\quad - (\alpha_i\mu_i + b_i)e_i. \end{aligned} \tag{32}$$

The total storage function is selected as $V_{\mathrm{ATBC}i} = V_{\mathrm{IIE}i} + T_i$. Taking the derivative of $V_{\mathrm{ATBC}i}$ and invoking (32) yield

$$\begin{aligned} \dot{V}_{\mathrm{ATBC}i} &= \dot{x}_i^T F_{\mathrm{H}i} - W_i + (1-\alpha_i\gamma_i)\delta_i \\ &\quad - \beta_i\sigma_i(1-\gamma_i)\delta_i - (\alpha_i\mu_i + b_i)e_i^T e_i \end{aligned} \tag{33}$$

where $W_i = (1-\alpha_i)\dot{x}_{\mathrm{VO}}^T B_{\mathrm{VO}}\dot{x}_{\mathrm{VO}} + (1-\alpha_i)e_i^T K_{\mathrm{P}i}e_i$, which is nonnegative.

The analysis of $\dot{V}_{\mathrm{ATBC}i}$ considers three cases based on γ_i and β_i, as detailed in Table I. For all cases, the inequality $\dot{V}_{\mathrm{ATBC}i} \leq \dot{x}_i^T F_{\mathrm{H}i}$ holds. Consequently, the IIE for *Operator #i* is passive with respect to $(F_{\mathrm{H}i}, \dot{x}_i)$. ■

It should be noted that in the second case of Table I, the nonpassive component $(1-\sigma_i)\delta_i$ is introduced by the EPR scheme. This term arises because the EPR scales only the energy transfer rate between the energy tank and the controller while preserving the task objectives ($\dot{x}_i \to \dot{x}_{\mathrm{VO}}$, $i = 1, 2, \ldots, n$). Thanks to the design of b_i, this issue is effectively addressed. The compensation term $b_i e_i^T e_i$ effectively addresses this issue and mitigates the EPR-induced tracking accuracy degradation, as proven in Section V.

Remark 2: When the tank energy reaches the lower limit $T_{\mathrm{MIN}i}$, the indeterminate relationship between the energy storage rate $\alpha_i P_{\mathrm{DISS}i}$ and the extraction rate P_i can cause fluctuations in tank energy near $T_{\mathrm{MIN}i}$, triggering chattering of β_i. This can lead to chattering in the control input, which further induces high-frequency noise in the velocity and degrades system stability. One common solution is to smooth β_i, which mitigates the resulting negative effects on system stability [33]. However, the proposed EPR scheme provides a fundamental alternative solution by preventing the depletion of tank energy.

Remark 3: From (19) and (31), a singularity occurs when $e_i^T e_i = 0$, which may cause dramatic change in control input and potentially degrade system stability. To avoid this issue, we replace (19) and (31) with

$$\mu_i = \begin{cases} \frac{\delta_i}{\alpha_i e_i^T e_i + \epsilon}, & \text{if } \gamma_i = 0 \text{ and } \beta_i = 0 \\ 0, & \text{otherwise} \end{cases} \tag{34}$$

and

$$b_i = \begin{cases} \frac{P_i - P_{\mathrm{MAX}i}}{P_i e_i^T e_i + \epsilon}\delta_i, & \text{if } P_i > P_{\mathrm{MAX}i} \geq 0 \\ 0, & \text{otherwise} \end{cases} \tag{35}$$

respectively, where ϵ is a designed positive constant. By setting a small ϵ, the impacts of such modification on IIE passivity could be effectively mitigated and even be negligible when $e_i^T e_i \gg \epsilon$. Furthermore, this modification cannot affect system stability. The corresponding analysis can refer to Section V.

V. CONVERGENCE ANALYSIS

This section focuses on the convergence of the tracking error e_i. The tracking error serves as a key metric for evaluating transparency in haptic rendering for the multiuser interaction.

IEEE Transactions on Robotics (T-RO) paper, presented at ICRA 2026, Vienna, Austria. Cite as T-RO paper.

Theorem 3: Under Assumptions 1 and 2, the problems defined in items 2) and 3) of Problem 2 are solved if $(1-\alpha_i)\underline{\lambda}_{K_{\mathrm{P}i}} - \frac{1}{2} > 0$, where $\underline{\lambda}_{K_{\mathrm{P}i}}$ represents the minimum eigenvalue of the matrix $K_{\mathrm{P}i}$.

Proof: 1) *Proof of Problem 2-2):* According to (3), Table I and Young's inequality, (33) can be calculated as

$$\begin{aligned}\dot{V}_{\mathrm{ATBC}i} &\le \dot{x}_i^T F_{\mathrm{H}i} - (1-\alpha_i) e_i^T K_{\mathrm{P}i} e_i \\ &= e_i^T F_{\mathrm{H}i} + \dot{x}_{\mathrm{VO}}^T F_{\mathrm{H}i} - (1-\alpha_i) e_i^T K_{\mathrm{P}i} e_i \\ &\le \frac{1}{2}\|\dot{x}_{\mathrm{VO}}\|^2 + \|F_{\mathrm{H}i}\|^2 - \left((1-\alpha_i)\underline{\lambda}_{K_{\mathrm{P}i}} - \frac{1}{2}\right)\|e_i\|^2.\end{aligned} \tag{36}$$

Based on (36), we can see that $\dot{V}_{\mathrm{ATBC}i} \le 0$ whenever

$$\|e_i\|^2 \ge \frac{1}{\rho_i}\left(\frac{1}{2}\|\dot{x}_{\mathrm{VO}}\|^2 + \|F_{\mathrm{H}i}\|^2\right) \tag{37}$$

where $\rho_i = (1-\alpha_i)\underline{\lambda}_{K_{\mathrm{P}i}} - \frac{1}{2}$. From Assumption 1 and (2), it follows that $\dot{x}_{\mathrm{VO}}$ is bounded. Therefore, the right-hand side of (37) is bounded. If (37) is satisfied, $\dot{V}_{\mathrm{ATBC}i}$ will be negative, causing $V_{\mathrm{ATBC}i}$ to decrease. As a result, by the definition of $V_{\mathrm{ATBC}i}$, the variables e_i, E_i and $\widetilde{\theta}_i$ will eventually decrease as well. When e_i decreases to

$$\|e_i\|^2 < \frac{1}{\rho_i}\left(\frac{1}{2}\|\dot{x}_{\mathrm{VO}}\|^2 + \|F_{\mathrm{H}i}\|^2\right). \tag{38}$$

$\dot{V}_{\mathrm{ATBC}i}$ will be positive. This leads to two possibilities. First, as $V_{\mathrm{ATBC}i}$ increases, e_i also increases. Once e_i reaches the bound defined in (37), $V_{\mathrm{ATBC}i}$ will begin to decrease. Consequently, if e_i continues to increase and decrease in this manner, e_i remains bounded, as do E_i and $\widetilde{\theta}_i$. The second possibility is that as $V_{\mathrm{ATBC}i}$ increases, e_i still remains within the bound defined in (38), while $\widetilde{\theta}_i$ and E_i increase. Combining the first possibility, e_i is proved to be bounded.

To ensure system stability, it is necessary to prove that $\widetilde{\theta}_i$ and E_i are bounded. From Remark 3, μ_i and b_i are bounded, and the above analysis establishes that e_i is bounded. By Assumption 1 and (2), $\dot{x}_{\mathrm{VO}}$, $\ddot{x}_{\mathrm{VO}}$, and $\dot{x}_i$ are also bounded. Since the practical operational workspace of the robot's end-effector is finite, Assumption 1 further ensures that E_i cannot grow unbounded. Therefore, the right-hand side of (32) and the terms $C_i(x_i,\dot{x}_i)e_i$, $D_i(x_i)$, and $Y_{\mathrm{d}i}(x_i,\dot{x}_i,\dot{x}_{\mathrm{VO}},\ddot{x}_{\mathrm{VO}})$ on the left-hand side are all bounded. It remains to prove $\widetilde{\theta}_i$ and $\dot{e}_i$ are bounded. If $\dot{e}_i$ is bounded, then so is $\widetilde{\theta}_i$ according to (32). Suppose that $\dot{e}_i$ goes to infinity, then $\|e_i\|$ will increase to the bound in (37), making $\dot{V}_{\mathrm{ATBC}i} \le 0$ and decreasing $V_{\mathrm{ATBC}i}$. As a result, e_i, E_i, and $\widetilde{\theta}_i$ decrease, and continually increase and decrease in this fashion. Hence, these variables remain bounded. From (32), $\dot{e}_i$ is bounded in this case, contradicting the infinity assumption. Therefore, both $\dot{e}_i$ and $\widetilde{\theta}_i$ are bounded, and the closed-loop system is stable.

2) *Proof of Problem 2-3):* If the ATBC is considered without the term related to b_i to compensate for the impacts of power regulation, it is rewritten as

$$u'_{\mathrm{ATBC}i} = u_{\mathrm{BASE}i} + u_{\mathrm{c}i} - \alpha_i\mu_i e_i. \tag{39}$$

Subsequently, when $P_i > P_{\mathrm{MAX}i} \ge 0$, (33) becomes

$$\begin{aligned}\dot{V}'_{\mathrm{ATBC}i} \le{}& \dot{x}_i^T F_{\mathrm{H}i} - (1-\alpha_i)\, e_i^T K_{\mathrm{P}i} e_i + (1-\alpha_i\gamma_i)\delta_i \\ &- \alpha_i\mu_i e_i^T e_i - \beta_i(1-\gamma_i)\frac{P_{\mathrm{MAX}i}}{P_i}\delta_i.\end{aligned} \tag{40}$$

Similar to the analysis of (33), (40) is calculated as

$$\begin{aligned}\dot{V}'_{\mathrm{ATBC}i} &\le \dot{x}_i^T F_{\mathrm{H}i} - (1-\alpha_i)\, e_i^T K_{\mathrm{P}i} e_i + \Delta_i \\ &\le \frac{1}{2}\|\dot{x}_{\mathrm{VO}}\|^2 + \|F_{\mathrm{H}i}\|^2 \\ &\quad - \left((1-\alpha_i)\underline{\lambda}_{K_{\mathrm{P}i}} - \frac{1}{2}\right)\|e_i\|^2 + \Delta_i\end{aligned} \tag{41}$$

where $\Delta_i = (1 - \frac{P_{\mathrm{MAX}i}}{P_i})\delta_i \ge 0$ is induced by the EPR scheme.

Similar to (36), it yields that $\dot{V}'_{\mathrm{ATBC}i} \le 0$ if

$$\|e_i\|^2 \ge \frac{1}{\rho_i}\left(\frac{1}{2}\|\dot{x}_{\mathrm{VO}}\|^2 + \|F_{\mathrm{H}i}\|^2 + \Delta_i\right) \tag{42}$$

and $\dot{V}'_{\mathrm{ATBC}i} > 0$ if

$$\|e_i\|^2 < \frac{1}{\rho_i}\left(\frac{1}{2}\|\dot{x}_{\mathrm{VO}}\|^2 + \|F_{\mathrm{H}i}\|^2 + \Delta_i\right). \tag{43}$$

Compared to the results in (37) and (38), it yields that Δ_i increases the boundary of e_i. However, under the same parameter settings for the virtual object and controllers, the design of b_i effectively compensates for the negative effects of power regulation on tracking accuracy. In addition, the analysis suggests that tracking performance can be further improved by increasing $K_{\mathrm{P}i}$. Specifically, by appropriately increasing the elements in $K_{\mathrm{P}i}$, the bound on $\|e_i\|$ can be reduced, thereby mitigating the increase of tracking error even when $F_{\mathrm{H}i}$ becomes large. ■

VI. Experimental Validation

In this section, experiments are performed in four different scenarios to validate the effectiveness of the proposed ATBC. Specifically, *Experiment #1* mainly compares the proposed ATBC with two state-of-the-art tank-based methods in terms of reproducibility and fidelity of haptic rendering. *Experiment #2* establishes a rigorous comparison environment to verify that the proposed EPR scheme can enhance control robustness to power limit settings, achieving a favorable tradeoff between IIE passivity and haptic fidelity. This result is further validated in *Experiment #3*, which involves a human–robot interaction scenario. Finally, *Experiment #4* demonstrates a clinical application of the ATBC, with a focus on rendering fidelity. All experiments involving human subjects were approved by the local ethics committee of the Southern University of Science and Technology (Approval No. 20230095), and consents were obtained from them.

A. Experimental Setup

The M-Hers used in experiments is shown in Fig. 5, consisting of three one-DOF haptic robots with identical configurations. A workstation PC, equipped with an Intel Core i5 9400F CPU (2.90 GHz), is connected to the three robots via USB cables. Each robotic setup is built on ESP32-S3 (Espressif Systems, Shanghai, PRC) and programmed on FreeRTOS with C code, operating at a frequency of 1 kHz. The interaction model is implemented via a virtual environment, created by the unity 3-D game engine (Unity Technologies, San Francisco, CA, USA). The end-effector velocity is computed by numerical differentiation of the position signal, derived from measured joint position via the transmission ratio, and applying a first-order low-pass filter (cut-off frequency of 64 Hz).

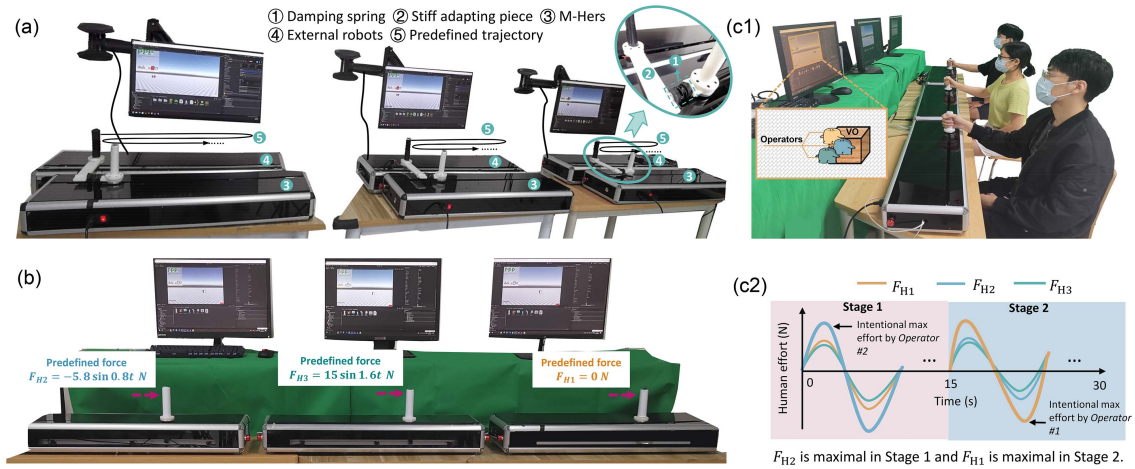

Fig. 5. System architecture of (a) *Experiment #1*, (b) *Experiment #2*, and (c1) *Experiment #3*. (c2) Task requirements for *Experiment #3*. In Stage 1, *Operator #2* exerts the largest force to dominate the task; in Stage 2, *Operator #1* takes over. The curves broadly depicts the contribution of human effort, instead the predefined force trajectory. VO denotes the virtual object.

For the considered setup, the dynamic model (1) is formulated as a one-DOF mass-damper system as follows:

$$D_i\ddot{x}_i + C_i\dot{x}_i = u_i + F_{\mathrm{H}i}, i = 1, 2, 3$$

where D_i and C_i are mass and damping terms, respectively.

The implemented TBC (18) is designed as

$$u_{\mathrm{TBC}i} = -K_{\mathrm{P}i}e_i - K_{\mathrm{I}i}E_i + Y_{\mathrm{d}i}\hat{\theta}_i + \beta_i(1-\gamma_i)\sum_{k=1}^{n}F_{Hk} - \alpha_i\mu_i e_i \tag{44}$$

with $\dot{\hat{\theta}}_i = -\Lambda_i Y_{\mathrm{d}i}^T e_i$, where $Y_{\mathrm{d}i} = [\ddot{x}_{\mathrm{VO}}, \dot{x}_{\mathrm{VO}}]$, and $\hat{\theta}_i = [\hat{D}_i, \hat{C}_i]^T$. $\hat{D}_i$ and $\hat{C}_i$ are the estimated values of D_i and C_i, respectively.

The implemented ATBC (30) is designed as

$$u_{\mathrm{ATBC}i} = -K_{\mathrm{P}i}e_i - K_{\mathrm{I}i}E_i + Y_{\mathrm{d}i}\hat{\theta}_i + \beta_i\sigma_i(1-\gamma_i)\sum_{k=1}^{n}F_{\mathrm{H}k} - (\alpha_i\mu_i + b_i)e_i. \tag{45}$$

Unless otherwise stated, the parameters of controller and interaction model used in all experiments are as follows: $K_{\mathrm{P}1} = K_{\mathrm{P}2} = K_{\mathrm{P}3} = 50$, $K_{\mathrm{I}1} = K_{\mathrm{I}2} = K_{\mathrm{I}3} = 1200$, $\Lambda_1 = \Lambda_2 = \Lambda_3 = \mathrm{diag}\{6, 60\}$, $T_{\mathrm{MIN}1} = T_{\mathrm{MIN}2} = T_{\mathrm{MIN}3} = 1.6$J, $T_{\mathrm{MAX}1} = T_{\mathrm{MAX}2} = T_{\mathrm{MAX}3} = 16$J, $\Delta t = 0.001$s, $T_1(0) = T_2(0) = T_3(0) = 8$J, $\alpha_1 = \alpha_2 = 0.33$, $\alpha_3 = 0.34$, $M_{\mathrm{VO}} = 30$ kg, and $B_{\mathrm{VO}} = 30$ Ns/m.

B. Experiment Design

In this section, the collaborative task of moving a shared virtual object was implemented under four scenarios.

1) Experiment #1: The performance of the proposed ATBC in addressing nonpassive human behaviors was evaluated by comparing it to two state-of-the-art controllers: the basic tank-based controller (BTC) [24] and valve-based tank-based controller (VTC) [32]. Following their design principles, we adapted their approaches to address the potentially nonpassive component δ_i identified in our work.

1) *Case #1* (BTC): This controller modifies the desired velocity command as

$$\dot{x}_{\mathrm{d}i} = (\gamma_i + (1-\gamma_i)\beta_i)\,\dot{x}_{\mathrm{VO}} + (1-\gamma_i)(1-\beta_i)\dot{x}'_{\mathrm{VO}i} \tag{46}$$

with $\dot{x}'_{\mathrm{VO}i}$ from $M_{\mathrm{VO}}\ddot{x}'_{\mathrm{VO}i} + B_{\mathrm{VO}}\dot{x}'_{\mathrm{VO}i} = F_{\mathrm{H}i}$. The position command $x'_{\mathrm{VO}i}$ is obtained by integration of $\dot{x}'_{\mathrm{VO}i}$. γ_i is designed as (14) and β_i is smoothly modified according to (26) in [24], given by

$$\beta_i = \begin{cases} 1, & \text{if } T_i \geq T_{\mathrm{MIN}i} + 0.6 \\ \frac{1}{2}\left(1 - \cos\left(\frac{T_i - T_{\mathrm{MIN}i}}{0.6}\pi\right)\right), & \text{if } T_{\mathrm{MIN}i} + 0.6 > T_i \geq T_{\mathrm{MIN}i} \\ 0, & \text{otherwise.} \end{cases}$$

2) *Case #2* (VTC): This controller augments BTC with CPR, and the desired velocity command is as follows:

$$\dot{x}_{\mathrm{d}i} = \sigma_i\,(\gamma_i + (1-\gamma_i)\beta_i)\,\dot{x}_{\mathrm{VO}} + (1-\gamma_i)(1-\beta_i)\dot{x}'_{\mathrm{VO}i} \tag{47}$$

where σ_i is designed following (25) in [32], which is same as (26) in the work but employs CPR with $P_{\mathrm{MAX}} = 2$. Other variables, including β_i and γ_i, are designed as same as those in *Case #1*.

3) *Case #3* (TBC): This is the proposed TBC (44) without power regulation.

4) *Case #4* (ATBC w/o b_i): The proposed ATBC (45) without b_i, using $k_{\max} = 2\Delta t$.

5) *Case #5* (ATBC): This is the full ATBC approach (45) with $k_{\max} = 2\Delta t$.

All the above cases were implemented under the identical experimental conditions for 10 trials. To ensure a consistent interaction environment, the M-Hers is mechanically coupled with three external robots that replace human operators by following predefined velocity trajectories, as shown in Fig. 5(a). The external robots serve as velocity sources and the connectors (i.e., stiff adapting piece and damping spring) provide passive mechanical behaviors. When the external robots move, the springs deform and generate interaction forces on the M-Hers. These forces consist of a voluntary component driven by the external robots' motion, and a passive component arising the connector, which aligns with Assumption 2.

TABLE II
POWER LIMIT SETTING IN *EXPERIMENTS #2* AND *#3*

Control Scheme	*Experiment #2*	*Experiment #3*
TBC (44)	✗	✗
ATBC (45) with CPR	$P_{\mathrm{MAXi}} = 4$	$P_{\mathrm{MAXi}} = 12$
	$P_{\mathrm{MAXi}} = 2$	$P_{\mathrm{MAXi}} = 8$
	$P_{\mathrm{MAXi}} = 1$	$P_{\mathrm{MAXi}} = 4$
	$P_{\mathrm{MAXi}} = 0.1$	$P_{\mathrm{MAXi}} = 2$
	–	$P_{\mathrm{MAXi}} = 1$
ATBC (45) with EPR as (27)	$k_{\max} = 0.05\Delta t$	$k_{\max} = 0.05\Delta t$
	$k_{\max} = 0.75\Delta t$	$k_{\max} = 0.75\Delta t$
	$k_{\max} = 2\Delta t$	$k_{\max} = 2\Delta t$
	$k_{\max} = 4\Delta t$	$k_{\max} = 4\Delta t$
	–	$k_{\max} = 8\Delta t$

- Δt denotes the sampling time ($\Delta t = 0.001$ in experiments)
- CPR: Constant Power Regulation, EPR: Exponential Power Regulation.
- ✗ denotes no power regulation.

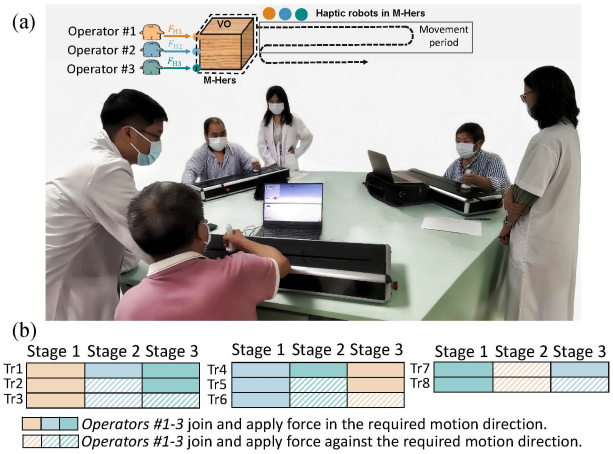

Fig. 6. (a) System architecture of *Experiment #4*. (b) Requirements of task participation in eight trials (Tr1–Tr8). Stage 1: One operator performs the task alone. Stage 2: A second operator joins. Stage 3: The third operator joins. Once joined, each operator continues participating in all subsequent stages. VO denotes the virtual object.

2) Experiment #2: This experiment includes nine scenarios, summarized in Table II, where all conditions remain same except for the upper bound of power $P_{\mathrm{MAX}i}$. Each scenario was repeated for 10 trials, and the results focus on the comparison between the proposed EPR approach and the CPR method (e.g., [32]). The experimental setup is shown in Fig. 5(b). Since operator forces are hard to keep consistent across trials, virtual operators with predefined forces were adopted to facilitate reliable comparison and statistical analysis. The predefined forces for virtual operators are set as $F_{\mathrm{H1}} = 0$ N, $F_{\mathrm{H2}} = -5.8\sin 0.8t$ N, and $F_{\mathrm{H3}} = 15\sin 1.6t$ N.

3) Experiment #3: Three healthy human operators (two male and one female: age 27.33 ± 2.52 years, weight 67 ± 14.1 kg, height 171.33 ± 10.07 cm) were recruited in this experiment, where they sat at the robots and grabbed the end-effector handles, as shown in Fig. 5(c1). The experiment simulates collaborative manipulation of moving a shared virtual object, whose motion arises from the operators' collective effort. The visual feedback shows the actual motion of the virtual object and robotic end-effectors, reflecting the control performance rather than a predefined trajectory to track. The task requirements are shown in Fig. 5(c2), indicating intended maximal forces at each stage and allowing operators to perceive assistance and resistance during the task. The identical procedure was implemented in 10 scenarios, categorized into CPR and EPR methods, as listed in Table II.

4) Experimental #4: To show the potential of the work for clinical applications, we conducted a clinical experiment in Shenzhen Second People's Hospital. In Fig. 6(a), three patients (two male and one female: age 54 ± 12.17 years, weight 74 ± 18.25 kg, height 163.33 ± 9.61 cm) with upper limb impairment collaboratively performed physical exercise in a shared virtual environment. The experiment series include eight trials of which patients sequentially joined the task with specified force directions, as illustrated in Fig. 6(b). They are designed to enable each patient perceive assistance or resistance from others in the collaborative task. In this experiment, $k_{\max} = 0.5\Delta t$.

C. Evaluation Method

The experiment results are evaluated regarding reproducibility, rendering fidelity, and robustness to power limit setting. Unless otherwise stated, the results are expressed as mean $\pm$ standard deviation (SD). $|\bar{(\cdot)}|$ denotes the absolute value of $\bar{(\cdot)}$, with $\bar{(\cdot)} = \frac{\sum_{\mathrm{tr}=1}^{\mathrm{Tr}}(\cdot)_{\mathrm{tr}}}{\mathrm{Tr}}$ being the average value of variable $(\cdot)$ across repeated trials, where $(\cdot)_{\mathrm{tr}}$ is the $(\cdot)$ in the trth trial, and Tr is the number of trials. The subscript i denotes $i = 1, 2, 3$.

1) Reproducibility: High reproducibility of haptic rendering, referring to the consistency of force-velocity behavior across repeated trials, is crucial for stable and repeatable task execution. It is rigorously examined using three indicators.

First, we calculate the normalized root mean square error (NRMSE) of interaction forces and their corresponding velocity response for each trial, using the average profiles across 10 trials ($\bar{F}_{\mathrm{H}i}$ and $\bar{\dot{x}}_i$) as baselines. The NRMSE is computed based on min–max normalization, i.e., $\mathrm{NRMSE}(F_{\mathrm{H}i}, \bar{F}_{\mathrm{H}i})$ and $\mathrm{NRMSE}(\dot{x}_i, \bar{\dot{x}}_i)$. Consistently small values across trials indicate low trial-to-trial variation and, thus, high reproducibility.

Second, we compute the SD of Spearman correlation coefficients between $F_{\mathrm{H}i}$ and $\dot{x}_i$ ($\mathrm{Corr}(F_{\mathrm{H}i}, \dot{x}_i)$) across trials to assess the consistency of the force-velocity relationship. The SD of $\mathrm{Corr}(F_{\mathrm{VO}}, \dot{x}_{\mathrm{VO}})$ is also analyzed to evaluate the consistency of virtual object rendering. A smaller SD value indicates more consistent results across trials, reflecting the reliability of haptic rendering.

Third, we analyze the concordance correlation coefficient (CCC) between each trial's interaction force and velocities and their baselines, i.e., $\mathrm{CCC}(F_{\mathrm{H}i}, \bar{F}_{\mathrm{H}i})$ and $\mathrm{CCC}(\dot{x}_i, \bar{\dot{x}}_i)$. Higher CCC values represent strong agreement and consistent force-velocity coupling behavior across trials.

2) Rendering Fidelity: The rendering fidelity is assessed using the trajectory tracking errors between M-Hers and virtual object. We analyze the integral absolute error (IAE) of the 2-norm of both $E = [E_1, E_2, E_3]$ and $e = [e_1, e_2, e_3]$, which treats all tracking errors equally and fully integrates their values and variations. In this work, it is defined as

$$\mathrm{IAE}_1(t) = \int_0^t \|\varpi(\tau)\| d\tau \tag{48}$$

where ϖ represents E and e, $t \in [0, t_{\mathrm{end}}]$ and t_{end} denotes the end time of a whole trial. Furthermore, we also introduce IAE_2

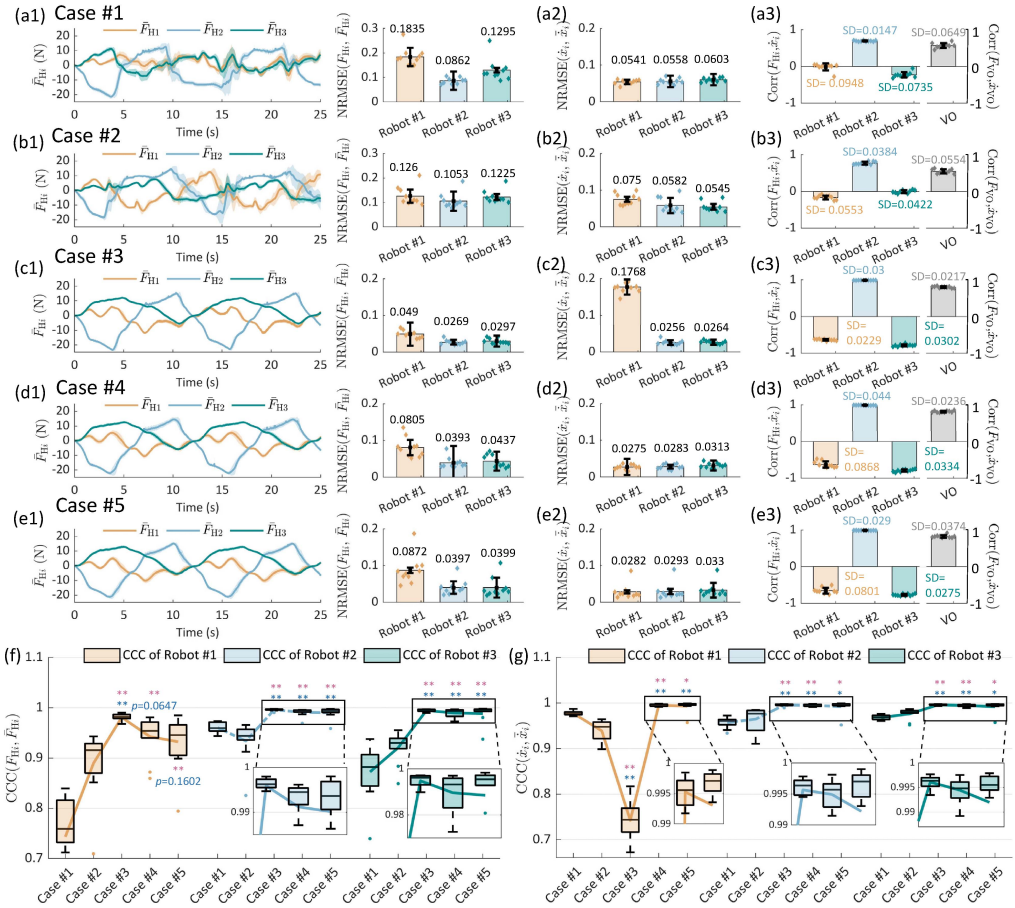

Fig. 7. *Experiment #1:* Validation of reproducibility. Average interaction force (curves), NRMSE based on min-max normalization (bars), and Spearman correlation coefficients (bars) for (a1)–(a3) *Case #1*, (b1)–(b3) *Case #2* (c1)–(c3) *Case #3*, (d1)–(d3) *Case #4*, and (e1)–(e3) *Case #5*. CCC values for (f) interaction forces and (g) corresponding velocity responses. The numbers in (a1)–(e1) and (a2)–(e2) are the mean NRMSE values. (a3)–(e3) Spearman correlation coefficient is denoted as Corr. SD denotes standard deviation. (f)–(g) Pink asterisk indicates a significant difference from *Case #1*, and the blue asterisk indicates a significance from *Case #2*.

for statistic analysis, which denotes the total accumulation of $\|\varpi(t)\|$ throughout the entire trial, as follows:

$$\mathrm{IAE}_2 = \int_0^{t_{\mathrm{end}}} \|\varpi(\tau)\| d\tau. \tag{49}$$

3) Robustness to Power Limit Setting: As discussed in Section IV-B, the power limit involves a tradeoff between control performance and IIE passivity. We, therefore, assess the controller's robustness to various power limit settings from both aspects. Since velocity is directly influenced by the control input and, thus, more sensitive to power regulation than position, the related metrics are calculated based on velocities. First, rendering accuracy is quantified using IAE_2, as described in Section VI-C2. Second, we examine the signal-to-noise ratio (SNR) of robot velocities during operation, which measures the ratio of desired signal power to noise power. As noted in Remark 2, high-frequency noise may be introduced into velocity signals when the tank energy approaches its lower bound, indicating that the IIE passivity is deteriorated. Thus, SNR is used to evaluate IIE passivity, with lower SNR values reflecting increased high-frequency noise

$$\mathrm{SNR} = 10 \lg \left(\frac{P_{\mathrm{desired}}}{P_{\mathrm{noise}}} \right) \tag{50}$$

where P_{desired} and P_{velocity} are the power of the reference velocity $\dot{x}_{\mathrm{VO}}$ and the actual measured velocity $\dot{x}_i$, respectively. $P_{\mathrm{noise}} = P_{\mathrm{velocity}} - P_{\mathrm{desired}}$ denotes the power of noise in the actual velocity, relative to the desired velocity.

4) Statistical Analysis: Based on the above metrics, statistical results were obtained using the Wilcoxon signed rank test ($p < 0.05$ is accepted as statistical significance). For multiple comparisons, the Benjamini–Hochberg correction was used to control the false discovery rate. In the corresponding plots, levels of statistical significance are indicated by asterisks as follows: ***$p < 0.001$, **$p < 0.005$, *$p < 0.05$; n.s. indicates no significant difference ($p \geq 0.05$).

D. Evaluation Results for Experiment #1

1) Reproducibility: Fig. 7 illustrates the reproducibility of haptic rendering under different methods. In Fig. 7(a1)–(e1), the mean NRMSE values for interaction forces under *Cases #3–#5* range from 0.0297 to 0.0872 (mean: 0.0484), which are notably lower than those in *Cases #1 and #2* (range from 0.0862 to 0.1835; mean: 0.1255). Fig. 7(f) further confirms the improved force reproducibility in *Cases #3–#5* through higher CCC. For example, the CCC values for *Robots #1–#3* are 0.9322 ± 0.0563, 0.9901 ± 0.0116, and 0.9885 ± 0.0187 in *Case #5*, with

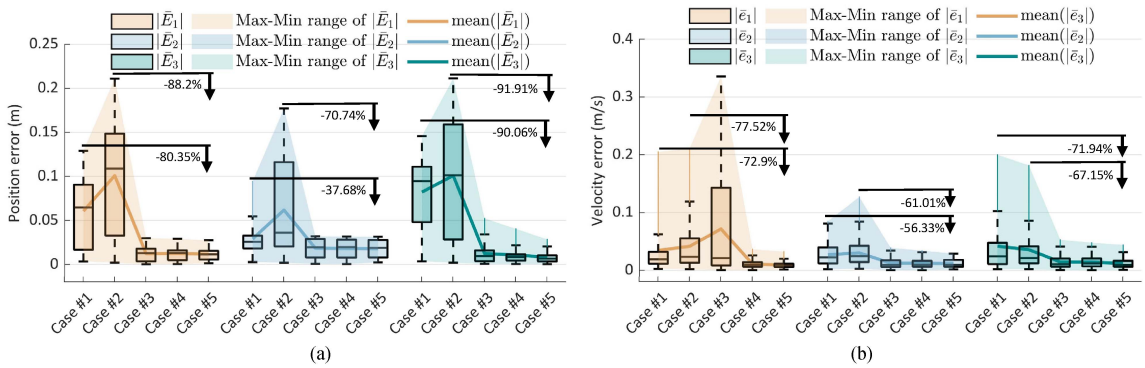

Fig. 8. *Experiment #1:* Validation of rendering fidelity: Distribution of the (a) absolute average position tracking error $|\bar{E}_i|$ and (b) absolute average velocity tracking error $|\bar{e}_i|$ across repeated trials under *Cases #1–#5*. The percentages are computed from the mean value of the absolute average errors (lines).

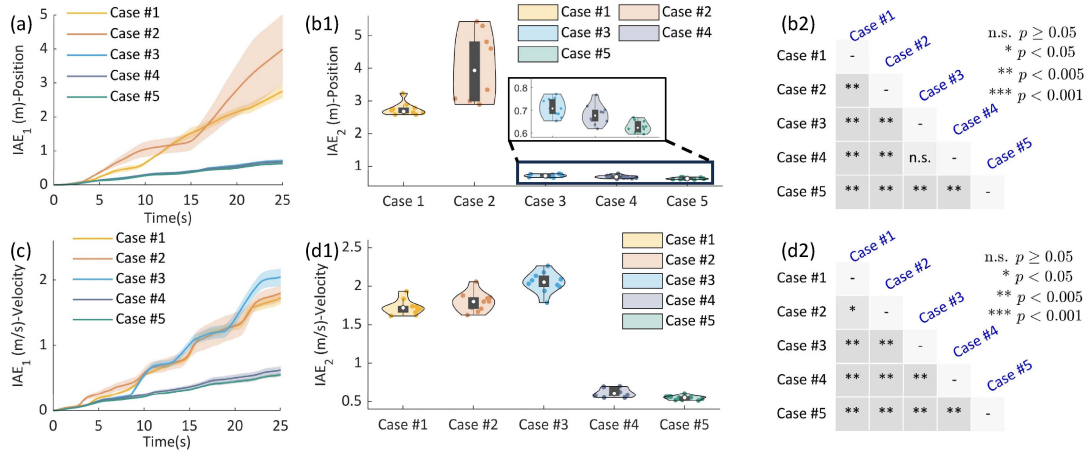

Fig. 9. *Experiment #1:* Validation of rendering fidelity: IAE under *Cases #1–#5*. (a) IAE_1, (b1) IAE_2, and its (b2) corresponding statistics based on $\|E\|$. (c) IAE_1, (d1) IAE_2, and (d2) its corresponding statistics based on $\|e\|$. The curves in (a) and (c) denote the average IAE_1 across trials, and the shaded regions represent the standard deviation.

improvements of 25.42%, 3.09%, and 13.31% over *Case #1* (all $p < 0.005$), and 4.78% ($p = 0.1602$), 6.03%, and 7.36% over *Case #2* (all $p < 0.005$ except *Robot #1*).

In Fig. 7(a2)–(e2), reproducibility enhancements are also observed in resultant robotic velocity response. *Cases #4 and #5* yield lower NRMSE (all ≤ 0.033) versus *Cases #1 and #2* (all ≥ 0.0541), along with significantly higher CCC. For example, in *Case #5*, CCC values for *Robots #1–#3* are 0.9931 ± 0.125, 0.9922 ± 0.143, and 0.992 ± 0.123, all significantly higher than those in *Cases #1 and #2* (all $p < 0.05$), as depicted in Fig. 7(g). Notably, $\bar{x}_1$ in *Case #3* exhibits high NRMSE due to its frequent oscillations caused by tank energy depletion, thereby reducing trial-to-trial consistency. This inference is shown in the results of TBC in *Experiments #2 and #3*.

In Fig. 7(a3)–(e3), *Case #5* demonstrates superior consistency in force-velocity coupling behavior compared to *Cases #1 and #2*. This is verified by its lower SD values of $\text{Corr}(F_{\text{H}i}, \dot{x}_i)$ (i.e., 0.0801, 0.029, and 0.0275 for *Robots #1–#3*) and a reduced SD values of $\text{Corr}(F_{\text{VO}}, \dot{x}_{\text{VO}})$ (0.0374; 42.37% and 32.49% reduction from *Cases #1* and *#2* respectively).

In summary, the proposed ATBC (*Case #5*) significantly enhances haptic rendering reproducibility over BTC (*Case #1*) and VTC (*Case #2*). A possible reason is the modified trajectory command in BTC and VTC [see (46) and (47)], where large deviations between $\dot{x}_{\text{VO}}$ and $\dot{x}'_{\text{VO}i}$ may cause aggressive transitions, leading to unpredictable robotic responses and degraded consistency. This effect is also evident in the Video 1, where slight oscillations in motion are observed under VTC.

2) Rendering Fidelity: Fig. 8(a) shows that the distribution of $|\bar{E}_i|$ in *Case #5* is 0.0119 ± 0.0073 m, 0.0181 ± 0.0098 m, and 0.0082 ± 0.0066 m for *Robots #1–#3*, with reductions up to 91.91% compared to *Cases #1 and #2*. Similarly, Fig. 8(b) presents that the $|\bar{e}_i|$ in *Case #5* yields 0.0093 ± 0.005 m/s, 0.0117 ± 0.0069 m/s, and 0.0117 ± 0.0077 m/s for *Robots #1–#3*, reducing by $\geq$56.33% compared to *Cases #1 and #2*. These improvements arise because the ATBC preserves the reference trajectory from virtual object as the desired command while ensuring IIE passivity via a time-varying control gain. In contrast, *Cases #1 and #2* enforce passivity by modifying the desired trajectory, leading to large deviations from the virtual object and degraded rendering accuracy. As shown in Fig. 9(a) and (c), IAE_1 values for $\|E\|$ and $\|e\|$ grows notably lower in *Cases #4 and #5* than in *Cases #1 and #2*. A similar result is observed in IAE_2 [see Fig. 9(b1) and (d1)], with significant difference ($p < 0.005$) listed in Fig. 9(b2) and (d2). Therefore, these findings demonstrate that the proposed ATBC achieves better rendering fidelity than conventional tank-based approaches.

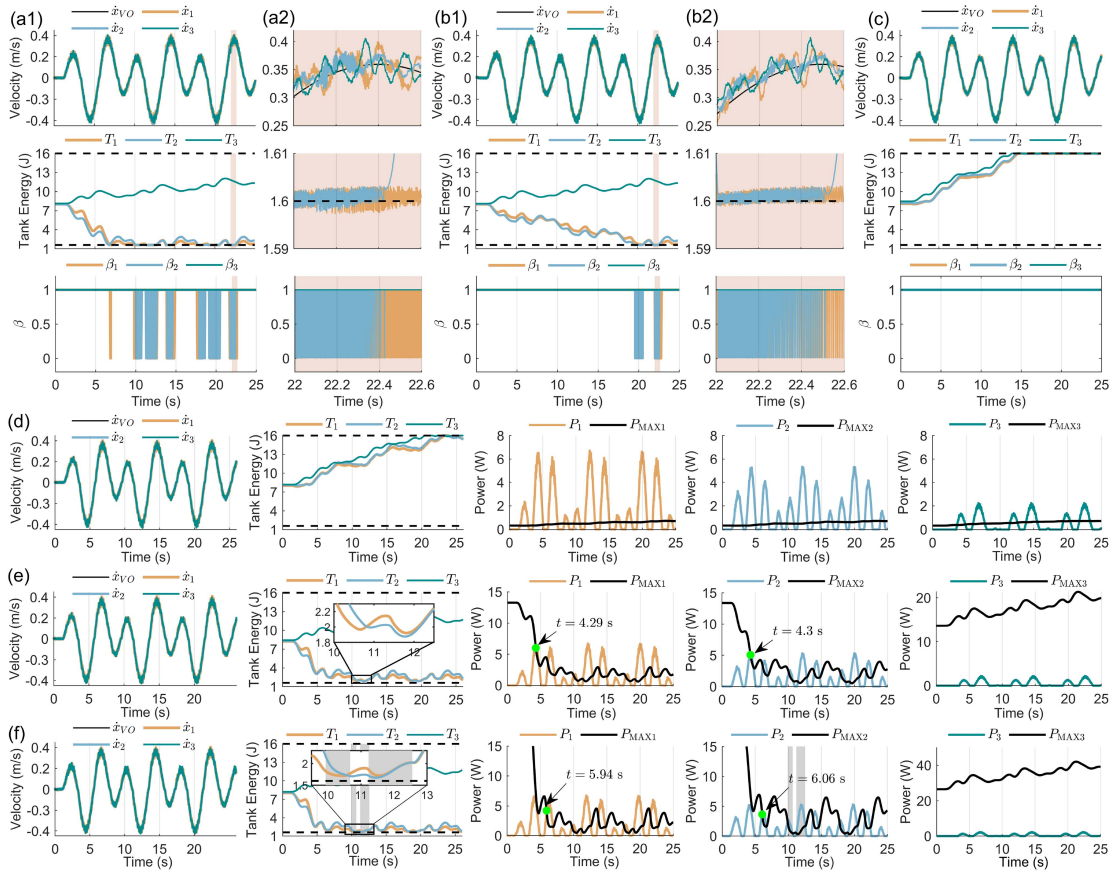

Fig. 10. *Experiment #2:* Evolution over time of tank energy T_i, β_i, and P_i $(i = 1, 2, 3)$ under (a) $P_{\text{MAX}} = 4$, (b) $P_{\text{MAX}} = 2$, (c) $P_{\text{MAX}} = 0.1$, (d) $k_{\max} = 0.05\Delta t$, (e) $k_{\max} = 2\Delta t$, and (f) $k_{\max} = 4\Delta t$. $P_{\text{MAX}} = P_{\text{MAX}i}$ $(i = 1, 2, 3)$. P_i represents the power without regulation. The green markers denote the moment when the power first reaches its limit. The shaded regions denote two adjacent intervals when power is limited.

Furthermore, *Case #5* achieves better tracking performance than *Case #4*, including the slower growth in IAE_1 and smallest values in IAE_2 for both position and velocity errors (all $p < 0.005$). These results reveal that the time-varying control gain b_i is helpful to enhance rendering accuracy.

Despite statistical difference, the increasing trend of IAE_1 for $\|E\|$ under *Case #3* is close to that under *Cases #4 and #5*, whereas *Case #3* exhibits higher IAE_2 for $\|e\|$. This is because the tank energy is depleted, and hence chattering is induced on velocity. Given no significant difference between *Cases #3* and for $\|E\|$, it can be inferred that position is more robust to tank energy depletion than velocity. This motivates the focus on velocity-based results in *Experiments #2 and #3*.

E. Evaluation Results for Experiment #2

1) EPR Scheme Analysis: The evolution of power is shown in Fig. 10(d)–(f), corresponding to different EPR settings of $k_{\max} = 0.05\Delta t$, $2\Delta t$, and $4\Delta t$, respectively. Two key results can be observed. First, a smaller EPR setting imposes a stricter limit on power flow. For example, under $k_{\max} = 0.05\Delta t$, power first reaches its bound much earlier ($t \approx 1.3$s for both P_1 and P_2) than under $k_{\max} = 2\Delta$ ($t = 4.29$ for P_1 and 4.3s for P_2) and $4\Delta t$ ($t = 5.94$ s for P_1, 6.06s for P_2). As a result, the tank energy (T_1 and T_2) continually increases, as shown in Fig. 10(d), because the strict power limit constrains energy extraction. By contrast, higher EPR settings allow more effective energy extraction, causing a reduction in tank energy, as shown in the curves of T_1 and T_2 in Fig. 10(e) and (f).

Second, the power limit $P_{\text{MAX}i}$ adapts to the real-time tank energy T_i as defined in (27). A higher T_i yields a larger $P_{\text{MAX}i}$, allowing greater power flow P_i and faster energy extraction. For instance, in Fig. 10(f), the largest EPR setting ($k_{\max i} = 4\Delta t$) leads to the lowest values of T_1 and T_2 at $t = 5$ s compared to other settings. As T_i drops, the $P_{\text{MAX}i}$ decreases, limiting P_i and slowing energy extraction. When the energy storage rate exceeds the extraction rate, T_i rises again, increasing $P_{\text{MAX}i}$ accordingly. This trend, highlighted by the shaded region in Fig. 10(f), demonstrates the regulation loop between T_i and $P_{\text{MAX}i}$ that prevents tank depletion and preserves system stability.

2) High-Frequency Noise: Fig. 10 shows the tank energy T_i, signal β_i, power P_i, and velocities $\dot{x}_i$ in a single trial under six scenarios. Fig. 10(a) and (b) depicts that overly large CPR settings ($P_{\text{MAX}i} = 4, 2$) lead to tank energy depletion, causing chattering in the β_i and velocities. In contrast, with a smaller power bound ($P_{\text{MAX}i} = 0.1$) in Fig. 10(c), T_i remains above the minimum energy limit $T_{\text{MIN}i}$, ensuring passive IIE and avoiding high-frequency noise in velocities. These results indicate that only CPR scheme with an appropriate bound can avoid tank energy depletion, as further confirmed by Fig. 11, where the SNRs for $\dot{x}_1$ and $\dot{x}_2$ increase as the $P_{\text{MAX}i}$ decreases. Using the EPR scheme, T_i always remains above its lower limit across different $k_{\max}$ settings, as displayed in Fig. 10(d)–(f). The corresponding

IEEE Transactions on Robotics (T-RO) paper, presented at ICRA 2026, Vienna, Austria. Cite as T-RO paper.

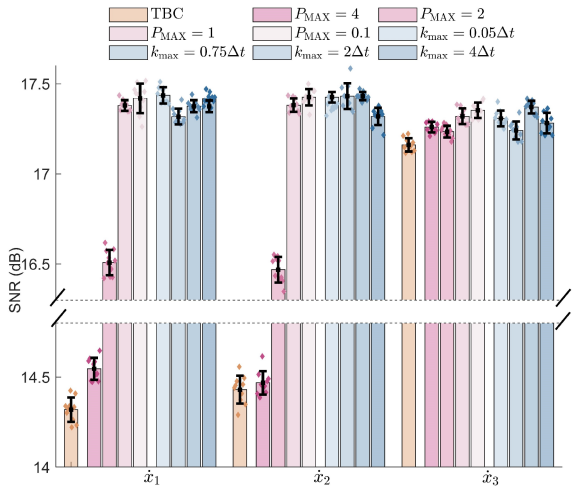

Fig. 11. *Experiment #2:* Validation of high-frequency noise: SNR. $P_{MAX} = P_{MAXi}$ $(i = 1, 2, 3)$.

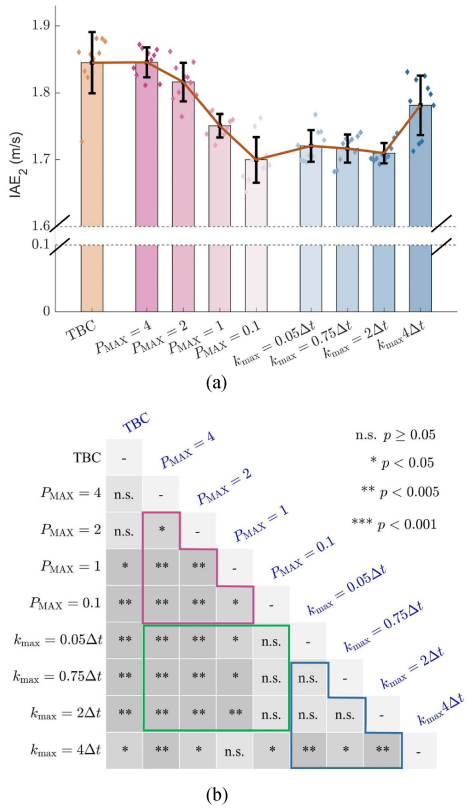

Fig. 12. *Experiment #2:* Validation of rendering fidelity: IAE of $\|e\|$ under different power regulation conditions. (a) Changes of IAE under scenarios with different power regulation. (b) Significant difference analysis of IAE. $P_{MAX} = P_{MAXi}$ $(i = 1, 2, 3)$.

SNRs for $\dot{x}_1$ and $\dot{x}_2$ exceed those using CPR scheme with high bounds (e.g., $P_{MAXi} = 4, 2$), as illustrated in Fig. 11. Therefore, the EPR scheme is more robust to power limit settings, as it can effective prevent tank energy depletion across a wide range of configurations.

3) Rendering Fidelity: Fig. 12(a) shows a significant reduction in IAE_2 as the CPR power upper bound decreases [$p < 0.05$ for pairwise comparisons in the pink frame in Fig. 12(b)]. This occurs because larger power bounds enable faster energy exchange between tank and controller, which can induce risky system behaviors. For example, Fig. 10 shows faster tank depletion under $P_{MAXi} = 4$ compared to $P_{MAXi} = 2$, leading to increased chattering in the signal β_i and higher velocity noise in $\dot{x}_1$ and $\dot{x}_2$. This observation aligns with the increased SNRs of $\dot{x}_1$ and $\dot{x}_2$ as P_{MAXi} decreases, as shown in Fig. 11. In contrast, IAE_2 shows no significant change across EPR cases ($k_{max} = 0.05\Delta t, 0.75\Delta t, 2\Delta t$; as highlighted in the blue frame of Fig. 12), with nearly identical SNR values in Fig. 11. These sharp contrasts suggest that EPR offers a better tradeoff between passivity and tracking performance compared to CPR, simplifying the selection of power bound and ensuring more reliable control outcomes.

The above claim is further substantiated by using $P_{MAXi} = 0.1$ and $k_{max} = 0.05\Delta t$ as the baseline. As shown in Fig. 10(c) and (d), the tank energy behavior under $P_{MAXi} = 0.1$ demonstrates stricter power regulation, with T_i reaching the upper limit T_{MAXi} in a shorter duration-15 s under $P_{MAXi} = 0.1$ versus more than 20 s under $k_{max} = 0.05\Delta t$. Despite this, there is no significant difference in rendering fidelity between these two cases ($p \geq 0.05$), as shown in Fig. 12(b). However, when the power bounds are increased 40-fold ($P_{MAXi} = 4$ and $k_{max} = 2\Delta t$, respectively), the system's behavior diverges significantly in terms of passivity and rendering fidelity. For instance, T_i reaches the lower limit under $P_{MAXi} = 4$, while remaining above the lower limit under $k_{max} = 2\Delta t$, as shown in Fig. 10(a) and (e). This indicates that the passivity condition of IIE is compromised under $P_{MAXi} = 4$. Furthermore, Fig. 12(b) reveals a significant difference in IAE_2 between $P_{MAXi} = 4$ and $P_{MAXi} = 0.1$, no significant difference between $k_{max} = 2\Delta t$ and $k_{max} = 0.05\Delta t$, and a significant difference between $P_{MAXi} = 4$ and $k_{max} = 2\Delta t$. These contrasts further validate the superior balance between IIE passivity and rendering accuracy achieved under the EPR method. Additional supporting results are highlighted in the green frame of Fig. 12(b).

The significant increase of IAE_2 under $k_{max} = 4\Delta t$ ($p < 0.05$ between $k_{max} = 4\Delta t$ and other three EPR cases listed in the blue frame) might be caused by the immense power exchange between energy tank and controller. In particular, overly relaxed power regulation can lead to dramatically changed control input, which would cause aggressive robot behavior and, thus, damage tracking performance.

F. Evaluation Results for Experiment #3

Fig. 13 displays the performance of TBC and ATBC, where velocities under TBC exhibit high-frequency noise, whereas ATBC maintains the stable motion throughout the operation. This distinction is validated by the power spectrum results, that is, the TBC generates higher power levels in the high-frequency range (200–500 Hz) compared to ATBC.

Fig. 14 presents the results under ten different power regulation conditions. Excessive CPR ($P_{MAXi} = 12$ and $P_{MAXi} = 8$) causes high-frequency noise, as shown in the power spectrum plots, leading to lower SNR values than other conditions. Fig. 14(d) shows that the tank energies reach their maximum limits within a similar time interval under $P_{MAXi} = 1$ ($t = 6.4s$) and $k_{max} = 0.05\Delta t$ ($t = 6s$), which indicates these two power limits regulate the rate of tank energy release at comparable levels. However, when the power limit increases eight-fold to

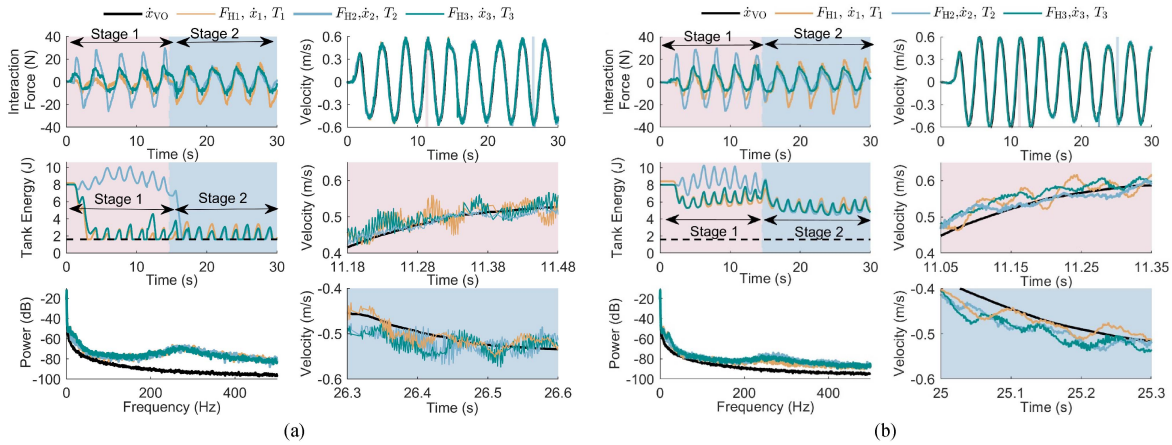

Fig. 13. *Experiment #3:* Evolution over time of tank energy T_i and β_i $(i = 1, 2, 3)$ and the resulting velocity under (a) TBC and (b) ATBC.

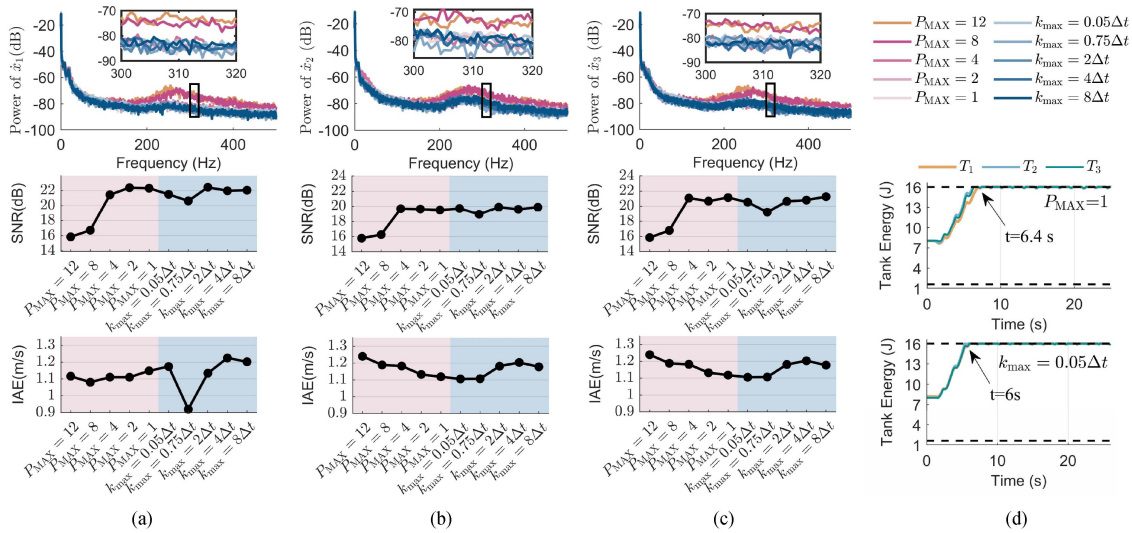

Fig. 14. *Experiment #3:* Validation of the impacts of different power regulation conditions on (a) *Robot #1*, (b) *Robot #2*, (c) *Robot #3*. (d) Tank energy evolution under $P_{\mathrm{MAX}} = 1$ and $k_{\mathrm{MAX}} = 0.05\Delta t$. $P_{\mathrm{MAX}} = P_{\mathrm{MAX}i}$ $(i = 1, 2, 3)$.

$P_{\mathrm{MAX}i} = 8$, the SNR values of velocities decrease substantially by 4–5 dB, as displayed in Fig. 14(a)–(c). In contrast, the SNR values remain nearly unchanged under EPR, demonstrating that this scheme relaxes the power bound selection for ensuring stable interaction. Furthermore, the tracking accuracy metric IAE_2 generally decreases as the power limit is reduced under both CPR and EPR schemes, further confirming that excessive power exchange would negatively affect tracking performance. In summary, the findings in *Experiment #3* are consistent with those of *Experiment #2*.

G. Evaluation Results for Experiment #4

In this experiment, all patients successfully completed the tasks without injury. Fig. 15 shows the interaction force profiles in two trials. In Fig. 15(a), the movement period (MP, the duration of one cycle as illustrated in Fig. 6(a) increases from 12.71 s (Stage 1) to 15.29 s (Stage 2), likely because F_{H2} in Stage 2 serves as resistance to *Operator #1*. In contrast, the MP in Stage 3 decreases to 7.6 s, as F_{H3} assists *Operator #1* by acting in the same direction as the virtual object's movement. Similar results can be observed in Fig. 15(b), where reduced MP corresponds to operators applying force aligned with the virtual object's motion. These findings suggest that the proposed ATBC enables collaborative task implementation in clinical scenarios.

Furthermore, despite irregular variations in interaction forces caused by patients' inconsistent motor outputs (see Fig. 15), the system maintained high fidelity. Fig. 16(a) shows the mean NRMSE for position tracking remains below 0.03 for all participants. Fig. 16(b) verifies that the mean NRMSE for velocity tracking remain below 0.06. These results demonstrate that the proposed ATBC maintains high rendering fidelity even under challenging interaction conditions.

VII. Conclusion

In this study, we focus on the scalability challenges in M-Hers with nonpassive human behaviors. To address this problem,

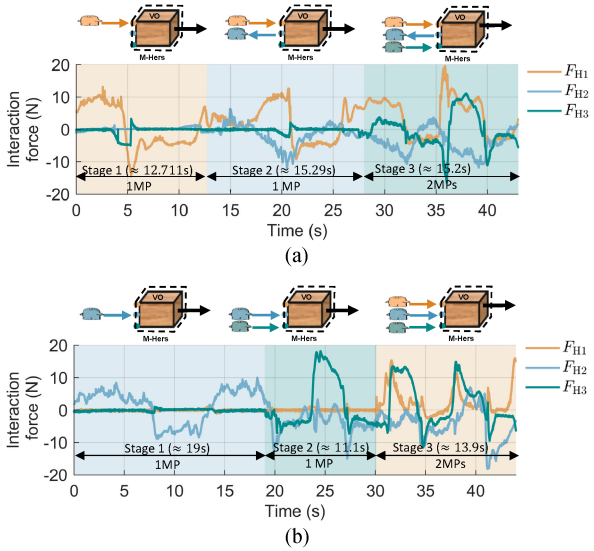

Fig. 15. *Experiment #4:* Interaction forces profiles in (a) Trial 2 (Tr 2) and (b) Trial 4 (Tr 4). MP denotes movement period, as illustrated in Fig. 6(a). VO denotes the virtual object.

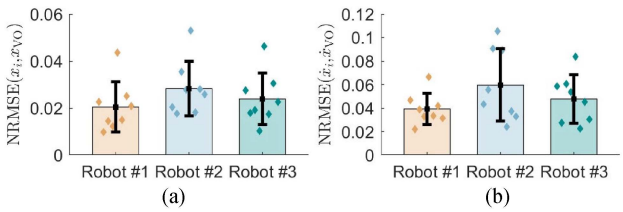

Fig. 16. *Experiment #4:* Validation of the rendering fidelity in terms of (a) NRMSE(x_i, x_{VO}), and (b) NRMSE$(\dot{x}_i, \dot{x}_{\mathrm{VO}})$. NRMSE denotes the NRMSE based on min–max normalization.

we propose an augmented tank-based control framework that includes two parts: 1) introducing the IIE to isolate the passivity-violated components caused by partners' active behaviors within each operator's workspace and 2) identifying these passivity violations within the IIE and designing an ATBC to ensure passive IIE. This proposed method effectively overcomes the challenges, such as complex stability conditions [7] and interaction coupling [8], [20], [21], [22], [23], by enabling independent ATBC design within each operator's IIE, thereby enhancing scalability and ensuring passive IIE.

The ATBC involves two critical efforts: first, rendering the multiuser interaction scenario that resembles real-world conditions while ensuring passive IIE; and second, enabling efficient tuning of power bound. The first goal is achieved by employing the EPR to only scale the power exchange between tank and controller, but remains the original task objectives. In other words, the desired command $\dot{x}_{\mathrm{VO}}$ from the interaction model is not modified, maintaining the authenticity of the haptic feedback. To further address potential resulting nonpassivity, we introduce a time-varying control gain b_i, which not only mitigates potential instability risk but also compensates for the impact of EPR on rendering fidelity. The second goal is achieved by the energy-related power bound adopted in EPR scheme. It effectively prevents the depletion of tank energy, avoiding potential unsafe system behaviors including chattering. Furthermore, this EPR mechanism enables a more flexible power bound range to ensure passive IIE than CPR [32], [33] and a lower computation cost compared to those utilizing optimization or learning algorithms [31], [35].

The effectiveness of the proposed ATBC was evaluated through four experimental scenarios, focusing on reproducibility, rendering accuracy, and robustness to power limit setting. First, *Experiment #1* showed that ATBC significantly improves both reproducibility and fidelity of haptic rendering compared to the BTC and VTC in [24], [32] (see Figs. 7–9) in addressing nonpassive human behaviors in IIE. The designed time-varying control gain b_i, formulated as (31), further enhances the rendering accuracy, as verified by the significant difference between ATBC and its variant without b_i (see Fig. 9). Second, *Experiments #2 and #3* proved that the EPR scheme significantly enhances the controller's robustness against varying power limit settings compared to CRP method, effectively preserving passivity and maintaining rendering quality (see Figs. 11, 12, and 14). Specifically, the EPR-based ATBC prevents the depletion of tank energy, thereby avoiding the chattering in both signal β_i and control input, and ensuring stable velocity response (see Figs. 10 and 13). In addition, rendering accuracy, quantified by IAE_2, shows statistical significance among CPR settings but remains statistically consistent across EPR settings (except at $k_{\max} = 4\Delta t$; see Fig. 12). Third, *Experiment #4* validated the clinical application of ATBC for collaborative task, verifying its ability of preserving high rendering fidelity despite irregular interaction forces from patients.

Although ATBC has been extensively validated through experiments for its effectiveness, its general applicability still requires further verification and expansion. Future experimental investigations will explore the effectiveness of the ATBC on M-Hers with multi-DOF robots or systems with different robotic dynamics. These studies are promising to provide more haptic-enabled interaction tasks in three-dimension space. Theoretically, further extensions will focus on addressing the impact of communication delays on the passivity of the IIE, making the proposed ATBC applicable to multiuser teleoperation systems. Another promising direction is to design a state observer for velocity and acceleration estimation that simultaneously guarantees IIE passivity, which could provide more stable estimate and better performance. These three future avenues hold the potential to expand the theoretical and practical scope of ATBC in complex scenarios.

Appendix A
Proof of Proposition 1

In the proof, we assume that the end effector of robots can perfectly tracking the position and velocity of virtual object, that is, $x_{\mathrm{VO}} = x_i$ and $\dot{x}_{\mathrm{VO}} = \dot{x}_i$, $i = 1, 2, \ldots, n$. For clarity, we proceed with the proof in one dimension as an example.

Proof:

Applying Laplace transformation to (2), we have

$$F_{\mathrm{VO}}(s) = Z_{\mathrm{VO}}(s) V_{\mathrm{VO}}(s) \tag{51}$$

where $Z_{\mathrm{VO}}(s) = M_{\mathrm{VO}} s + B_{\mathrm{VO}}$ is the impedance of virtual object, $V_{\mathrm{VO}}(s) = sX_{\mathrm{VO}}(s)$.

For *Operator #i*, there exists

$$F_{\mathrm{H}i}(s) = Z_i(s) V_{\mathrm{VO}}(s) \tag{52}$$

where $Z_i(s)$ denotes the impedance felt by *Operator #i*.

Due to $F_{\text{VO}}(t) = \sum_{i=1}^{n} F_{\text{H}i}(t)$, and by combing (51) and (52), the following holds:

$$Z_{\text{VO}}(s) = \sum_{i=1}^{n} Z_i(s). \tag{53}$$

Based on (51)−(53), we obtain

$$\frac{F_{\text{H}i}(s)}{F_{\text{VO}}(s)} = \frac{Z_i(s)}{Z_{\text{VO}}(s)}. \tag{54}$$

If $F_{\text{H}i}(s), i = 1, 2, \ldots, n$ at sample time t_k evolves to $F_{\text{H}i}^{NEW}(s) = F_{\text{H}i}(s) + \Delta F_{\text{H}i}(s)$ at the subsequent sample time t_{k+1}, then (54) becomes

$$\frac{F_{\text{H}i}^{\text{NEW}}(s)}{F_{\text{VO}}(s) + \sum_{j=1}^{n} \Delta F_{\text{H}j}(s)} = \frac{Z_i^{\text{NEW}}(s)}{Z_{\text{VO}}(s)} \tag{55}$$

where the subscript j is used as a summation index to avoid confusion with the fixed operator index i.

From (54) and (55), we define the changed impedance felt by *Operator #i* as

$$\begin{aligned}\Delta Z_i(s) &= Z_i^{\text{NEW}}(s) - Z_i(s) \\ &= \left(\frac{F_{\text{H}i}^{\text{NEW}}(s)}{F_{\text{VO}}(s) + \sum_{j=1}^{n} \Delta F_{\text{H}j}(s)} - \frac{F_{\text{H}i}(s)}{F_{\text{VO}}(s)} \right) Z_{\text{VO}}(s) \\ &= \frac{F_{\text{VO}}(s)\Delta F_{\text{H}i}(s) - F_{\text{H}i}(s)\sum_{j=1}^{n} \Delta F_{\text{H}j}(s)}{F_{\text{VO}}(s)F_{\text{VO}}(s) + F_{\text{VO}}(s)\sum_{j=1}^{n} \Delta F_{\text{H}j}(s)} Z_{\text{VO}}(s).\end{aligned} \tag{56}$$

To ensure $\Delta Z_i(s) = 0$, the condition should be satisfied such that for any $\Delta F_{\text{H}i}(s)$, $F_{\text{VO}}(s)\Delta F_{\text{H}i}(s) - F_{\text{H}i}(s)\sum_{j=1}^{n} \Delta F_{\text{H}j}(s) = 0$. This implies that the changed interaction forces $F_{\text{H}i}(s)$ should meet the following requirement:

$$\frac{F_{\text{H}i}(s)}{F_{\text{VO}}(s)} = \frac{\Delta F_{\text{H}i}(s)}{\sum_{j=1}^{n} \Delta F_{\text{H}j}(s)}. \tag{57}$$

The condition in (57) is challenging to fulfill because $\sum_{j=1}^{n} \Delta F_{\text{H}j}(s)$ includes the voluntary contributions of partners, as described in Assumption 2. Given that regulating operators' voluntary contributions is almost impossible, it can be inferred that the impedance felt by *Operator #i* will vary with changes in partners' interaction forces. ■

Appendix B
Proof of Proposition 2

Proof: In multiuser collaborative haptic-enabled interaction, the movement of all operators is in the same direction. Taking the IIE for *Operator #i* $\in \{1, 2, \ldots, n\}$ as an example, an IIE satisfies

$$\dot{x}_i^T(t) F_{Hi}(t) = \dot{V}_i(t) + W_i(t)$$

with $W_i(t) = W_{Si}(t) + W_{Pi}(t)$. Here, $V_i(t)$ is the stored energy in the ith IIE, $W_{Si}(t) \geq 0$ denotes the power dissipated by the controlled system, and $W_{Pi}(t)$ is the power dissipated or injected by the partners in IIE of the ith human operator. If $W_{Pi}(t) > 0$, the partners within the ith IIE dissipate energy; otherwise, they will inject energy into the IIE.

On the one hand, if $W_{Pi}(t) > 0$, the partners' forces oppose the movement of *Operator #i*. In this case, the movement of *Operator #i* is resisted, and the condition $W_{Si}(t) + W_{Pi}(t) > 0$ holds. Thus, the passivity of the ith IIE will be ensured.

On the other hand, if $W_{Pi}(t) < 0$, the partners will inject active energy to the ith IIE, which means that their forces support or are at least consistent with the movement of *Operator #i*. In this case, the ith human operator could maintain the current velocity with less force or achieve larger velocity with the same force. As a result, the movement is assisted. According to the definition of passivity, once the condition $W_{Si}(t) + W_{Pi}(t) < 0$ holds, the passivity of the ith IIE will be violated. ■

Appendix C
Proof of Fig. 3

Proof: According to Assumption 2, the model of passive component F_{PAS1} is $Z_{\text{H1}}(\bullet)$, we can obtain that

$$\dot{S}_{\text{H1}} \leq \dot{x}_1^T F_{\text{PAS1}}$$

where S_{H1} is the storage function of the passive component.

Suppose Σ_2 is passive, it yields that

$$\dot{S}_{\Sigma_2} \leq \dot{x}_1^T F_{\text{H1}}$$

where S_{Σ_2} is the storage function of Σ_2.

Taking $S_{\Sigma_3} = S_{\text{H1}} + S_{\Sigma_2}$ as the storage function for the feedback interconnection between $Z_{\text{H1}}(\bullet)$ and Σ_2 in Σ_3, and based on $F_{\text{VOL1}} = F_{\text{PAS1}} + F_{\text{H1}}$ as stated in Assumption 2, we have

$$\dot{x}_1^T F_{\text{VOL1}} \leq \dot{S}_{\text{H1}} + \dot{S}_{\sigma_3}.$$

Therefore, the passivity of Σ_2 suffices the passivity of Σ_3. ■

Acknowledgment

The authors would like to thank the rehabilitation physicians in Shenzhen Second People's Hospital, Changlong Huang, and Jie Guo for their assistance in clinical trials, and Yahui Hao and Rui Ma in helping revise the manuscript.

References

[1] M. Shahbazi, S. F. Atashzar, H. A. Talebi, and R. V. Patel, "Novel cooperative teleoperation framework: Multi-master/single-slave system," *IEEE/ASME Trans. Mechatron.*, vol. 20, no. 4, pp. 1668–1679, Apr. 2015.

[2] A. Jazayeri, M. Dyck, and M. Tavakoli, "Stability analysis of teleoperation systems under strictly passive and non-passive operator," in *Proc. World Haptics Conf.*, 2013, pp. 695–700.

[3] S. F. Atashzar, I. G. Polushin, and R. V. Patel, "Networked teleoperation with non-passive environment: Application to tele-rehabilitation," in *Proc. IEEE/RSJ Int. Conf. Intell. Robots Syst.*, 2012, pp. 5125–5130.

[4] A. Van Der Schaft, *Passive State Space Systems*. Cham, Switzerland: Springer, 2017, pp. 59–99.

[5] Y. Yang, D. Constantinescu, and Y. Shi, "Passive multiuser teleoperation of a multirobot system with connectivity-preserving containment," *IEEE Trans. Robot.*, vol. 38, no. 1, pp. 209–228, Jan. 2022.

[6] T. Kastritsi, T. P. Semetzidis, and Z. Doulgeri, "Passive bilateral surgical teleoperation with RCM and spatial constraints in the presence of time delays," *IEEE Trans. Robot.*, vol. 41, pp. 612–627, 2025.

[7] R. Tao and M. Tavakoli, "Multilateral haptic system stability analysis: The effect of activity or passivity of terminations via a series-shunt approach," in *Proc. IEEE Haptics Symp.*, 2014, pp. 203–208.

[8] S. F. Atashzar, M. Shahbazi, M. Tavakoli, and R. V. Patel, "A new passivity-based control technique for safe patient-robot interaction in haptics-enabled rehabilitation systems," in *Proc. IEEE/RSJ Int. Conf. Intell. Robots Syst.*, 2015, pp. 4556–4561.

[9] V. Mendez and M. Tavakoli, "A passivity criterion for N-port multilateral haptic systems," in *Proc. 49th IEEE Conf. Decis. Control*, 2010, pp. 274–279.

[10] J. Li, M. Tavakoli, V. Mendez, and Q. Huang, "Conservatism of passivity criteria for stability analysis of trilateral haptic systems," in *Proc. World Haptics Conf.*, 2013, pp. 633–638.

[11] V. Mendez, M. Tavakoli, and J. Li, "A method for passivity analysis of multilateral haptic systems," *Adv. Robot.*, vol. 28, no. 18, pp. 1205–1219, 2014.

[12] J. Li, M. Tavakoli, V. Mendez, and Q. Huang, "Passivity and absolute stability analyses of trilateral haptic collaborative systems," *J. Intell. Robot. Syst.*, vol. 78, pp. 3–20, 2015.

[13] T. Kanno and Y. Yokokohji, "Multilateral teleoperation control over time-delayed computer networks using wave variables," in *Proc. IEEE Haptics Symp.*, 2012, pp. 125–131.

[14] R. Rakhsha and D. Constantinescu, "Passive shared virtual environment for distributed haptic cooperation," in *Proc. IEEE Haptics Symp.*, 2014, pp. 221–226.

[15] M. Panzirsch, J. Artigas, J.-H. Ryu, and M. Ferre, "Multilateral control for delayed teleoperation," in *Proc. 16th Int. Conf. Adv. Robot.*, 2013, pp. 1–6.

[16] M. Panzirsch, R. Balachandran, and J. Artigas, "Cartesian task allocation for cooperative, multilateral teleoperation under time delay," in *Proc. IEEE Int. Conf. Robot. Autom.*, 2015, pp. 312–317.

[17] J.-H. Ryu, Q. Ha-Van, and A. Jafari, "Multilateral teleoperation over communication time delay using the time-domain passivity approach," *IEEE Trans. Control Syst. Technol.*, vol. 28, no. 6, pp. 2705–2712, Jun. 2020.

[18] H. Van Quang and J.-H. Ryu, "Stable multilateral teleoperation with time domain passivity approach," in *Proc. IEEE/RSJ Int. Conf. Intell. Robots Syst.*, 2013, pp. 5890–5895.

[19] A. Jazayeri and M. Tavakoli, "Revisiting llewellyn's absolute stability criterion for bilateral teleoperation systems under non-passive operator or environment," in *Proc. IEEE/RSJ Int. Conf. Intell. Robots Syst.*, 2012, pp. 70–75.

[20] S. F. Atashzar, M. Shahbazi, M. Tavakoli, and R. V. Patel, "A grasp-based passivity signature for haptics-enabled human-robot interaction: Application to design of a new safety mechanism for robotic rehabilitation," *Int. J. Robot. Res.*, vol. 36, no. 5–7, pp. 778–799, 2017.

[21] S. F. Atashzar, M. Shahbazi, M. Tavakoli, and R. V. Patel, "A passivity-based approach for stable patient– robot interaction in haptics-enabled rehabilitation systems: Modulated time-domain passivity control," *IEEE Trans. Control Syst. Technol.*, vol. 25, no. 3, pp. 991–1006, Mar. 2017.

[22] S. Thudi and S. F. Atashzar, "Discrete windowed-energy variable structure passivity signature control for physical human-(tele)robot interaction," *IEEE Robot. Autom. Lett.*, vol. 6, no. 2, pp. 3647–3654, Feb. 2021.

[23] P. Paik, S. Thudi, and S. F. Atashzar, "Power-based velocity-domain variable structure passivity signature control for physical human-(tele)robot interaction," *IEEE Trans. Robot.*, vol. 39, no. 1, pp. 386–398, Jan. 2023.

[24] S. Haddadin and E. Shahriari, "Unified force-impedance control," *Int. J. Robot. Res.*, vol. 43, no. 13, pp. 2112–2141, 2024.

[25] F. Ferraguti et al., "A variable admittance control strategy for stable physical human–robot interaction," *Int. J. Robot. Res.*, vol. 38, no. 6, pp. 747–765, 2019.

[26] Z. Li, H. Wei, H. Zhang, and C. Liu, "A variable admittance control strategy for stable and compliant human-robot physical interaction," *IEEE Robot. Autom. Lett.*, vol. 10, no. 2, pp. 1138–1145, Feb. 2025.

[27] B. Capelli, C. Secchi, and L. Sabattini, "Passivity and control barrier functions: Optimizing the use of energy," *IEEE Robot. Autom. Lett.*, vol. 7, no. 2, pp. 1356–1363, Feb. 2022.

[28] C. Secchi, A. Franchi, H. H. Bülthoff, and P. R. Giordano, "Bilateral teleoperation of a group of UAVs with communication delays and switching topology," in *Proc. IEEE Int. Conf. Robot. Autom.*, 2012, pp. 4307–4314.

[29] A. Franchi, C. Secchi, H. I. Son, H. H. Bulthoff, and P. R. Giordano, "Bilateral teleoperation of groups of mobile robots with time-varying topology," *IEEE Trans. Robot.*, vol. 28, no. 5, pp. 1019–1033, May 2012.

[30] A. Dietrich, X. Wu, K. Bussmann, C. Ott, A. Albu-Schäffer, and S. Stramigioli, "Passive hierarchical impedance control via energy tanks," *IEEE Robot. Autom. Lett.*, vol. 2, no. 2, pp. 522–529, Feb. 2017.

[31] Y. Michel, C. Ott, and D. Lee, "Safety-aware hierarchical passivity-based variable compliance control for redundant manipulators," *IEEE Trans. Robot.*, vol. 38, no. 6, pp. 3899–3916, Jun. 2022.

[32] M. Brunner, L. Giacomini, R. Siegwart, and M. Tognon, "Energy tank-based policies for robust aerial physical interaction with moving objects," in *Proc. Int. Conf. Robot. Autom.*, 2022, pp. 2054–2060.

[33] E. Shahriari, L. Johannsmeier, and S. Haddadin, "Valve-based virtual energy tanks: A framework to simultaneously passify controls and embed control objectives," in *Proc. Annu. Amer. Control Conf.*, 2018, pp. 3634–3641.

[34] F. Benzi, M. Brunner, M. Tognon, C. Secchi, and R. Siegwart, "Adaptive tank-based control for aerial physical interaction with uncertain dynamic environments using energy-task estimation," *IEEE Robot. Autom. Lett.*, vol. 7, no. 4, pp. 9129–9136, Apr. 2022.

[35] E. Shahriari, L. Johannsmeier, E. Jensen, and S. Haddadin, "Power flow regulation, adaptation, and learning for intrinsically robust virtual energy tanks," *IEEE Robot. Autom. Lett.*, vol. 5, no. 1, pp. 211–218, Jan. 2020.

[36] F. Benzi and C. Secchi, "Unified power and admittance adaptation for safe and effective physical interaction with unmodelled dynamic environments," *IEEE Robot. Autom. Lett.*, vol. 8, no. 12, pp. 8279–8286, Dec. 2023.

[37] M. Bednarczyk, H. Omran, and B. Bayle, "Passivity filter for variable impedance control," in *Proc. IEEE/RSJ Int. Conf. Intell. Robots Syst.*, 2020, pp. 7159–7164.

[38] E. Spyrakos-Papastavridis, P. R. N. Childs, and J. S. Dai, "Passivity preservation for variable impedance control of compliant robots," *IEEE/ASME Trans. Mechatron.*, vol. 25, no. 5, pp. 2342–2353, May 2020.

[39] S. F. Atashzar, I. G. Polushin, and R. V. Patel, "A small-gain approach for nonpassive bilateral telerobotic rehabilitation: Stability analysis and controller synthesis," *IEEE Trans. Robot.*, vol. 33, no. 1, pp. 49–66, Jan. 2017.

[40] S. Chiaverini and B. Siciliano, "On the stability of a force/position control scheme for robot manipulators," *IFAC Proc. Volumes*, vol. 24, no. 9, pp. 183–188, 1991.

[41] J.-J. E. Slotine and W. Li, *Applied Nonlinear Control*, vol. 199, no. 1. Englewood Cliffs, NJ, USA: Prentice-Hall, 1991.

[42] P. Paik, X. Zhou, and S. F. Atashzar, "Hierarchical frequency-based energy separation in variable structure control for robot-mediated human–human interaction," *IEEE Trans. Instrum. Meas.*, vol. 74, 2025, Art. no. 7508814.

[43] S. Cremer, S. K. Das, I. B. Wijayasinghe, D. O. Popa, and F. L. Lewis, "Model-free online neuroadaptive controller with intent estimation for physical human–robot interaction," *IEEE Trans. Robot.*, vol. 36, no. 1, pp. 240–253, Jan. 2020.

[44] R. Nomberg and I. Nisky, "Human-in-the-loop stability analysis of haptic rendering with time delay—The effect of delayed feedback control in the operator model," *IEEE Robot. Autom. Lett.*, vol. 8, no. 10, pp. 6379–6386, Oct. 2023.

[45] J. Luo, C. Zhang, W. Si, Y. Jiang, C. Yang, and C. Zeng, "A physical human–robot interaction framework for trajectory adaptation based on human motion prediction and adaptive impedance control," *IEEE Trans. Autom. Sci. Eng.*, vol. 22, pp. 5072–5083, 2025.

[46] B. Brogliato et al., "Dissipative systems analysis and control," *Theory Appl.*, vol. 2, pp. 2–5, 2007.

Cui Wang received the B.Eng. degree in electrical engineering and the M.Eng. degree in control science and engineering from the University of Jinan, Jinan, China, in 2016 and 2019, respectively. She is currently working toward the Ph.D. degree in mechanical engineering with the Department of Mechanical Engineering, City University of Hong Kong, Hong Kong.

Her research interests include haptic control and human–robot interaction.

Yudong Liu received the master's degree in engineering from the Department of Biomedical Engineering, Southern University of Science and Technology, Shenzhen, China, in 2024.

He is currently a Research Assistant with the Department of Biomedical Engineering, Southern University of Science and Technology. His research areas include rehabilitation robotics and physical human–robot interaction.

Chenyang Sun (Member, IEEE) received the M.Sc. degree in advanced robotics from the Department of Advanced Robotics, Ecole Centrale de Nantes, Nantes, France, in 2019 and the Ph.D. degree in biomedical engineering from the Department of Biomedical Engineering, Southern University of Science and Technology, Shenzhen, China, in 2025.

She is currently a Postdoctoral Researcher with the Department of Biomedical Engineering, Harbin Institute of Technology, Shenzhen, China. Her research areas include rehabilitation robotics and physical human–robot interaction.

Ping Li (Member, IEEE) received the B.S. degree in mechanical engineering and automation from the South China University of Technology, Guangzhou, China, in 2011, and the Ph.D. degree in mechanical and electronic engineering from the Huazhong University of Science and Technology, Wuhan, China, in 2019.

He is currently a Research Assistant Professor with the Southern University of Science and Technology, Shenzhen, China. His research interests include CNC system, mechatronics, system modeling and identification, motion control, robot control, and fully actuated system approach.

Yi-Feng Chen (Member, IEEE) received the M.Sc. degree in information and communication engineering and Ph.D. degree in communication and information systems from the School of Information Engineering, Wuhan University of Technology, Wuhan, China, in 2014 and 2017, respectively.

He has completed a Postdoctoral Fellowship with joint appointment from the Academy for Advanced Interdisciplinary Studies and the Department of Biomedical Engineering, Southern University of Science and Technology, Shenzhen, China, in 2023. He is currently a Research Assistant Professor with the Southern University of Science and Technology, Shenzhen, China. His research areas include biomedical signal processing, brain–computer interfaces, rehabilitation robotics, and artificial intelligence.

Mingjie Dong (Senior Member, IEEE) received the B.E. degree in mechanical engineering and automation from the School of Mechanical Engineering and Automation, Beihang University, Beijing, China, in 2012, and the Ph.D. degree in mechatronics engineering from the Robotics Institute, Beihang University in March 2018.

He is currently an Associate Professor with the College of Mechanical and Energy Engineering, Beijing University of Technology, Beijing, China. His current research includes rehabilitation robotics and physical human–robot interaction control.

Dr. Dong was an Invited Reviewer for many high-quality international journals, such as IEEE TRANSACTIONS ON AUTOMATION SCIENCE AND ENGINEERING, IEEE/ASME TRANSACTIONS ON MECHATRONICS, and IEEE TRANSACTIONS ON INDUSTRIAL ELECTRONICS.

Zhenhong Li (Senior Member, IEEE) received the B.Eng. degree in electrical engineering from the Huazhong University of Science and Technology, Wuhan, China, in 2014, and the M.S. and Ph.D. degrees in control engineering from the University of Manchester, Manchester, U.K., in 2019.

From 2019 to 2023, he was a Research Fellow in Rehabilitation Robotics with the University of Leeds, Leeds, U.K. Since 2023, he has been a Lecturer in Robotics and Control with the University of Manchester. His research interests include human–robot interaction, rehabilitation robotics, and neuromuscular interface.

Lu Liu (Senior Member, IEEE) received the Ph.D. degree in mechanical and automation engineering from the Department of Mechanical and Automation Engineering, Chinese University of Hong Kong, Hong Kong, in 2008.

From 2009 to 2012, she was an Assistant Professor with The University of Tokyo, Tokyo, Japan, and then with the University of Nottingham, Nottingham, U.K. She then joined the City University of Hong Kong, where she is currently a Professor. Her primary research interests include networked systems, multirobot systems, and intelligent control.

Dr. Liu was an Associate Editor for IEEE TRANSACTIONS ON CYBERNETICS, IEEE TRANSACTIONS ON FUZZY SYSTEMS, IEEE ROBOTICS AND AUTOMATION LETTERS, *Control Theory and Technology*, and *Unmanned Systems*.

Mingming Zhang (Senior Member, IEEE) received the Ph.D. degree in mechanical engineering from the University of Auckland, Auckland, New Zealand, in 2015.

Following his Ph.D., he held Research Fellow and Visiting Research Fellow with the Department of Mechanical Engineering, University of Auckland. In August 2018, he joined the Southern University of Science and Technology, Shenzhen, China, as an Assistant Professor, and was promoted to Associate Professor in 2024. He has authored more than 120 academic articles and holds more than 50 patents. His research interests include medical and rehabilitation robotics, haptic control, human–robot physical interaction, and brain–computer interfaces.

Dr. Zhang is currently an Associate Editor for IEEE TRANSACTIONS ON NEURAL SYSTEMS AND REHABILITATION ENGINEERING, IEEE ROBOTICS AND AUTOMATION LETTERS, and IEEE TRANSACTIONS ON MEDICAL ROBOTICS AND BIONICS.